

Environmental and coastline changes controlling Holocene carbon accumulation rates in fjords of the western Strait of Magellan region

Ríos Francisco ^{1,*}, Kilian Rolf ^{1,2}, Lange Carina B. ^{3,4,5,6}, Baeza-Urrea Oscar ¹, Arz Helge W. ⁷, Zindorf Mark ⁸, De Pol-Holz Ricardo ⁹, Lamy Frank ¹⁰

¹ Universität Trier, Lehrstuhl für Geologie Fachbereich Geographie/Geowissenschaften (FB VI), Campus II, Behringstrasse 21, 54286, Trier, Deutschland

² Universidad de Magallanes, Avenida Bulnes, 01855, Punta Arenas, Chile

³ Departamento de Oceanografía, Universidad de Concepción, Casilla 160-C, Concepción, Chile

⁴ Centro de Investigación Oceanográfica COPAS Sur-Austral, Universidad de Concepción, Barrio Universitario, Concepción, Chile

⁵ Centro de Investigación Dinámica de Ecosistemas Marinos de Altas Latitudes (IDEAL), Universidad Austral de Chile, Campus Isla Teja, Valdivia, Chile

⁶ Scripps Institution of Oceanography, La Jolla, California, 92037, USA

⁷ Leibniz-Institut für Ostseeforschung Warnemünde, Seestraße 15, 18119, Rostock-Warnemünde, Deutschland

⁸ Ifremer - Centre de Brest, Laboratoire Environnement Profond, 29280, Plouzané, France

⁹ Centro de Investigación GAIA-Antártica (CIGA) and Network for Extreme Environment Research (NEXER), Universidad de Magallanes, Avenida Bulnes, 01855, Punta Arenas, Chile

¹⁰ Alfred-Wegener-Institut Helmholtz-Zentrum für Polar und Meeresforschung, 27570, Bremerhaven, Deutschland

* Corresponding author : Francisco Rios, email address : phrano@gmail.com

clang@udec.cl ; baezaurr@uni-trier.de ; helge.arz@io-warnemuende.de ; mark@zindorf.de ; ricardo.depol@umag.cl ; Frank.Lamy@awi.de

Abstract :

Organic-rich sediments of the southernmost Chilean Pacific coast and its fjord system constitute an important component of the global marine carbon budget. Sediment records from Trampa and Caribe bays and Churruca fjord in the western Magellan fjord system have been analyzed with the goal of understanding the factors controlling carbon accumulation and its regional fluctuation throughout the Holocene. The individual response in paleoproductivity at the different sites and related variations in accumulation rates document a very complex interplay among local and regional-scale environmental changes, and coastline elevation across the Holocene. Shallow sill basins close to the Pacific coast, as the ones studied here, are particularly sensitive to these processes, having responded with strong productivity changes throughout the Holocene.

A Bayesian mixed model approach, using sediment archived provenance proxies, indicates that components of terrestrial plants and soils washed-out into these basins contribute with a variable

proportion (20 to 80 wt%) of the total accumulated organic carbon. Accumulation rates of terrestrial carbon increase with the amount of precipitation in the hyper-humid mountain area, but also reflect distinct Holocene plant successions as well as long-term development of soil and vegetation cover that strongly overprint the direct precipitation impact. Over the Holocene accumulation rates of biogenic carbonate and aquatic-marine organic carbon range between 5 to 118 kg m⁻² kyr⁻¹ and 0.3 to 20 kg m⁻² kyr⁻¹, respectively. This variability depends on water column structure and conditions, which are regulated by the degree of marine transgression as a function of post glacial sea level rise and isostatic uplift as well as precipitation-related surface water freshening. In the Bahia Trampa record, a significant change in accumulation rates indicates a marine transgression at ca. 12.2 kyr BP, when the global sea level was 60–70 m lower than today and eustatic rise overcame isostatic rebound rates. In Caribe and Trampa records, CaCO₃ accumulation rates were higher at ca. 7 kyr BP. The Churruca record shows organic carbon accumulation rates up to 36.2 kg m⁻² kyr⁻¹ during the early Holocene.

Highlights

► Holocene accumulation rates of terrestrial carbon in Patagonian fjords are influenced by local environmental conditions such as precipitation regime, catchment/basin area ratio, and, soil and vegetation development. ► The accumulation rates of carbonate and aquatic organic carbon in coastal sites with shallow-sills are controlled by the interaction between sea level variations and isostatic adjustments. ► The marine transgression at Bahia Trampa site indicates a total isostatic rebound of 60–70 m for the north-western Strait of Magellan.

Keywords : Patagonian fjord sediments, paleoproductivity, carbon accumulation, biogenic carbonate, marine transgression, Holocene.

72 **1. Introduction**

73 The factors controlling fluxes and coastal aquatic-marine storage of organic carbon (OC) as
74 well as the accumulation of biogenic carbonate in shelf sediments, and particularly in fjord
75 regions, are crucial for the global carbon budget. A recently review highlights the importance
76 of these sensitive systems needing intensive investigation (Bianchi et al., 2020). Smith et al.
77 (2015) estimated that the contribution of OC in fjord sediments is equivalent to ~10 wt% of
78 the annual marine OC burial. The Pacific continental margin of Patagonia includes the most
79 extended fjord region in the world (total area of 240,000 km² and 84,000 km of coastline;
80 Pantoja et al., 2011). Despite its vast extension, only few studies constrain the recent
81 accumulation of aquatic-marine and terrestrial OC, and biogenic carbonate in sediments of
82 the Patagonian fjord ecosystems (Aracena et al., 2011; Lafon et al., 2014; Sepúlveda et al.,
83 2011; Silva et al., 2011; Vargas et al., 2011). The spatial distribution of OC sources of north
84 Patagonia surface sediments indicate a gradient of terrestrial OC contents from 62 wt% to 32
85 wt% in a fjord-ocean transect (González et al., 2019).

86 On longer time-scales, Holocene fjord sediment records show variable contribution of
87 OC from terrestrial vegetation sources, in particular derived from dense rainforests and
88 peatlands (OC_{terr}: 30 to 70 wt%; Bertrand et al., 2017 and 2012; Harada et al., 2013; Lamy et
89 al., 2010; Rebolledo et al., 2015). The amount of terrestrial input to these fjord sediments
90 depends on local and regional factors. Local geomorphology, in particular ratios between the
91 areas of terrestrial catchments and related fjord basins (Cui et al., 2017, Hinojosa et al.,
92 2014, Smeaton and Austin, 2017), development of drainage conditions as well as long-term
93 development of soils with distinct chemical compositions related to bedrock lithologies, play a
94 major role. Regional to local factors as climate conditions and the altitudinal distribution of
95 the vegetation zone influence the transport of OC_{terr}, which often depends on precipitation
96 rates and locally associated water pathways (Lamy et al., 2010). Moreover, damages of
97 terrestrial ecosystems after the deposition of tephra from explosive volcanic eruptions cause
98 enhanced plant decay up to a millennium scale leading to increased delivery and deposition
99 of OC_{terr} (Kilian et al., 2006; Korup et al., 2019; Mohr et al., 2017).

100 Organic carbon from aquatic-marine sources (OC_{aq}) in Patagonian fjords principally
101 derives from the local production of “brackish water” organic matter, which is related to sea
102 surface temperatures (SSTs), the supply of nutrients, and the depth of the photic zone
103 (Cuevas et al., 2019; Kilian et al., 2013a). Macronutrients (nitrate and phosphate) are mainly
104 introduced by oceanic water with higher salinities and locally reduced thermohaline gradients
105 (Cuevas et al., 2019; Ríos et al., 2016). Moreover, continental runoff transports other
106 macronutrients such as dissolved silica as well as micronutrients (i.e., iron) into the fjords,
107 exerting an additional influence on the “brackish water” productivity (Iriarte et al., 2014;
108 Torres et al., 2011, 2014).

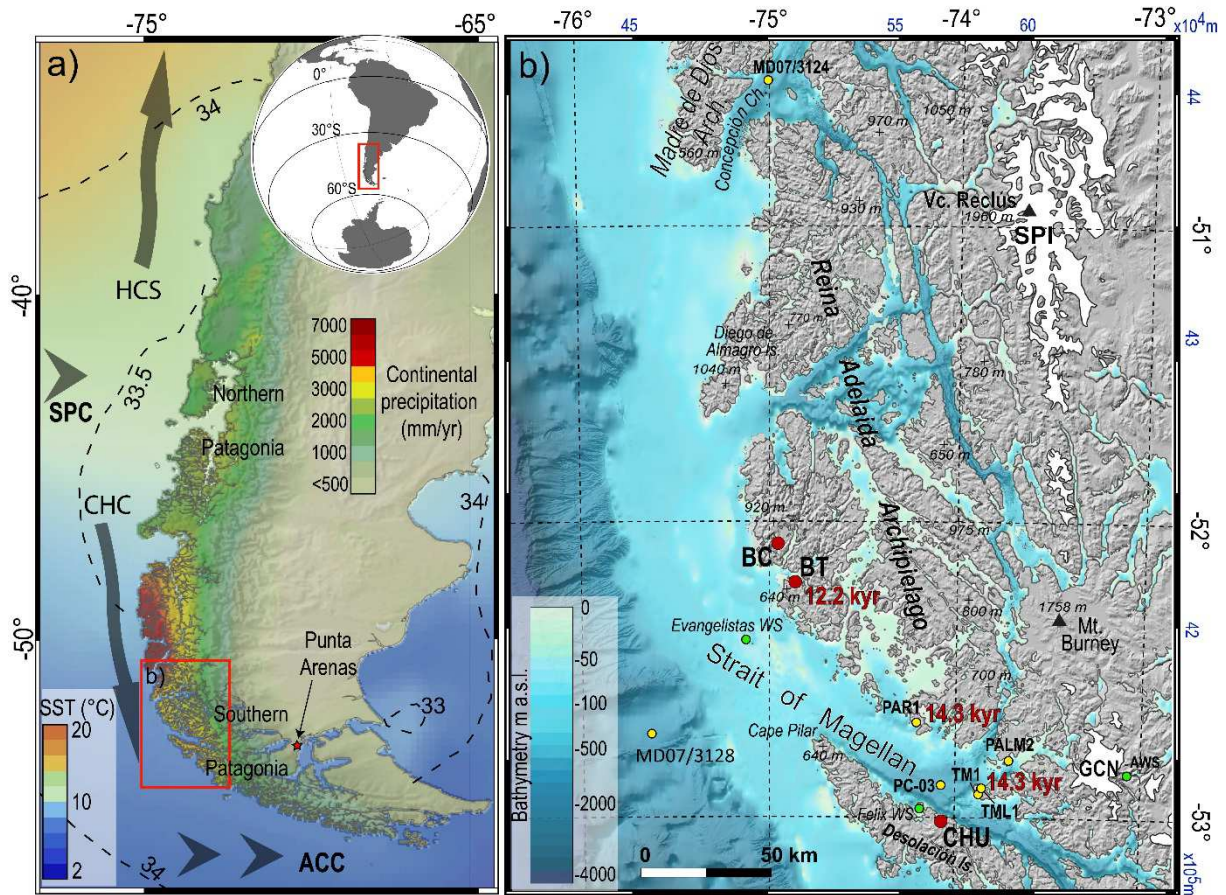
109 A significant amount of carbon storage in fjord sediments concerns the accumulation
110 of biogenic carbonate that contributes to the total carbon burial with a regionally and
111 temporally highly variable quantity (Smeaton et al., 2017). Since accumulation of biogenic
112 carbonate in fjords is sourced from planktic and benthic organisms, the relative contribution
113 of both depends on thermohaline and nutrient conditions within the whole water column
114 (González et al., 2013; Milzer et al., 2013; Rüggeberg et al., 2016). In particular, benthic
115 foraminifera constitute up to 38 wt% of the inorganic carbon in Arctic fjord sediments
116 (Pawłowska et al., 2017). In the Magellan fjord system, benthic foraminifera species
117 distribution is strongly controlled by oceanic input from the Pacific in the west and the
118 freshwater input from land (Hromic et al., 2006). This freshwater input occurs as a superficial
119 outflow, which in addition to variations in runoff from rivers and streams, and meltwater from
120 glaciers, is controlled by the variable strength of the Southern Westerly Winds (SWW) (Kilian
121 et al., 2013a).

122 Variability in SWW intensities exhibit a significant positive correlation with the amount
123 of precipitation on the elevated windward side of the Andes (Garreaud et al., 2013), and thus
124 also with the freshwater discharge and local glacier mass balances. The related physical and
125 chemical denudation rates control the terrestrial supply of micronutrients (Breuer et al.,
126 2013a) and consequently, affect the aquatic primary production in the fjord region (Kilian et
127 al., 2013a; Ríos et al., 2016). Based on the correlation between precipitation and regional
128 SWW intensities, precipitation-sensitive proxies in sediment cores have been used to
129 reconstruct Holocene variations in width, strength and latitudinal position of the SWW belt
130 (Kilian and Lamy, 2012 and references therein).

131 Records from southwestern Patagonia (52°–53°S) evidence highest precipitation
132 rates during the early Holocene between ca. 11 to 8.5 kyr BP (Kilian and Lamy 2012; Lamy
133 et al., 2010). These implications have been partially controversially discussed (Moreno et al.,
134 2010; Fletcher and Moreno, 2012). At these latitudes, recent studies from eastern Patagonia,
135 which presents an inverse correlation between precipitation and zonal wind intensities
136 (Garreaud et al., 2013), indicate a humid phase in the early Holocene between ca. 11.2 to
137 10.1 kyr BP while increased SWW intensity occurred from ca.10.1–8.3 kyr BP (Zolitschka et
138 al., 2019). Composite analysis of pollen data from sites east of the Andes support the
139 hypothesis that storm tracks weakened throughout Patagonia (41°–55°S) between ca.13–10
140 kyr BP, followed by stronger storm tracks in southern Patagonia than in northern Patagonia
141 between ca.10–7 kyr BP (Nanavati et al., 2019).

142 In this context, records from the westernmost fjord region may contribute to a better
143 understanding of the long-term variability and location of the SWW during the Late Glacial
144 and the Holocene (Aracena et al., 2015; Harada et al., 2013). Here, we present three new
145 sediment records from the fjord region around the western sector of the Strait of Magellan

146 (Fig. 1a). The investigated cores represent examples of regional variations in accumulation
 147 rates and aquatic paleoproductivity since the Late Glacial. More specifically, we use organic
 148 and inorganic geochemical proxies and physical properties of the sediment cores with the
 149 aim of understanding the evolution and control factors of OC accumulation. We further infer
 150 the effects of marine transgression and the related coastline changes on marine productivity
 151 and OC accumulation as well as biogenic carbonate burial in the southern Patagonian fjords.



152
 153 **Figure 1:** a) Southernmost South America with average annual precipitation values over
 154 Patagonia (mm yr^{-1} ; New et al., 2001), and modern annual mean sea surface temperature
 155 (SST °C) and salinity (dashed lines in psu) distributions of the surrounding ocean (WOA13,
 156 Boyer et al., 2013). Modern ocean surface currents after Strub et al. (2019) include the South
 157 Pacific Current (SPC), the northward-branching Humboldt Current System (HCS),
 158 southward-branching Cap Horn Current (CHC) and the Antarctic Circumpolar Current (ACC).
 159 The red rectangle indicates the study area shown in Fig. 1b. b) Red circles refer to the
 160 location of the new sediment core sites Bahía Trampa (BT), Bahía Caribe (BC) and Churruca
 161 fjord (CHU) presented here. Yellow circles show the position of core sites discussed in the
 162 text, and green circles refer to weather stations (WS) and the automatic weather station near
 163 Gran Campo Nevado ice field (AWS). Red annotations in kyr indicate the minimum age for
 164 the marine transgression in the western sector of the Strait of Magellan (after Lamy et al.,

165 *2010 and Kilian et al., 2007a). Topography and bathymetry from GMRT 3.5 (Ryan et al.,*
166 *2009). Blue annotation indicates the UTM coordinates. Projection UTM18S, datum WGS84.*

167 **2. Study area**

168 Next to the Pacific entrance of the Strait of Magellan there is an extended water system with
169 estuarine characteristics that serves as an important transition area between land and ocean
170 environments, including fjords, estuaries and other coastal semi-enclosed ecosystems. The
171 infilled postglacial sediments represent valuable archives for reconstructing past
172 environmental changes in this region including paleoproductivity. The site-specific
173 productivity and sedimentation dynamics strongly depend on local bathymetries of variably
174 deep basins and subaquatic sills (Table 1), which at present control – and during the past
175 constrained – the influence of open marine water masses and a westward expanding surface
176 outflow of fresher water from the inner fjords.

177 2.1. Description of sites

178 The locations of the investigated sediment cores are shown in Fig. 1b. Two of them are
179 located in the southwestern sector of the Reina Adelaida Archipelago, next to the Pacific
180 Ocean within previously unnamed small bays on the Contreras and Pacheco islands, now
181 denominated Bahía Caribe and Bahía Trampa, respectively (Fig. 2a). These areas should
182 have experienced pronounced regional coastline changes during the Holocene. A third
183 sediment core was retrieved from the Churruca fjord, which is located to the southeast of the
184 other two sites at Desolación Island (Fig. 2b).

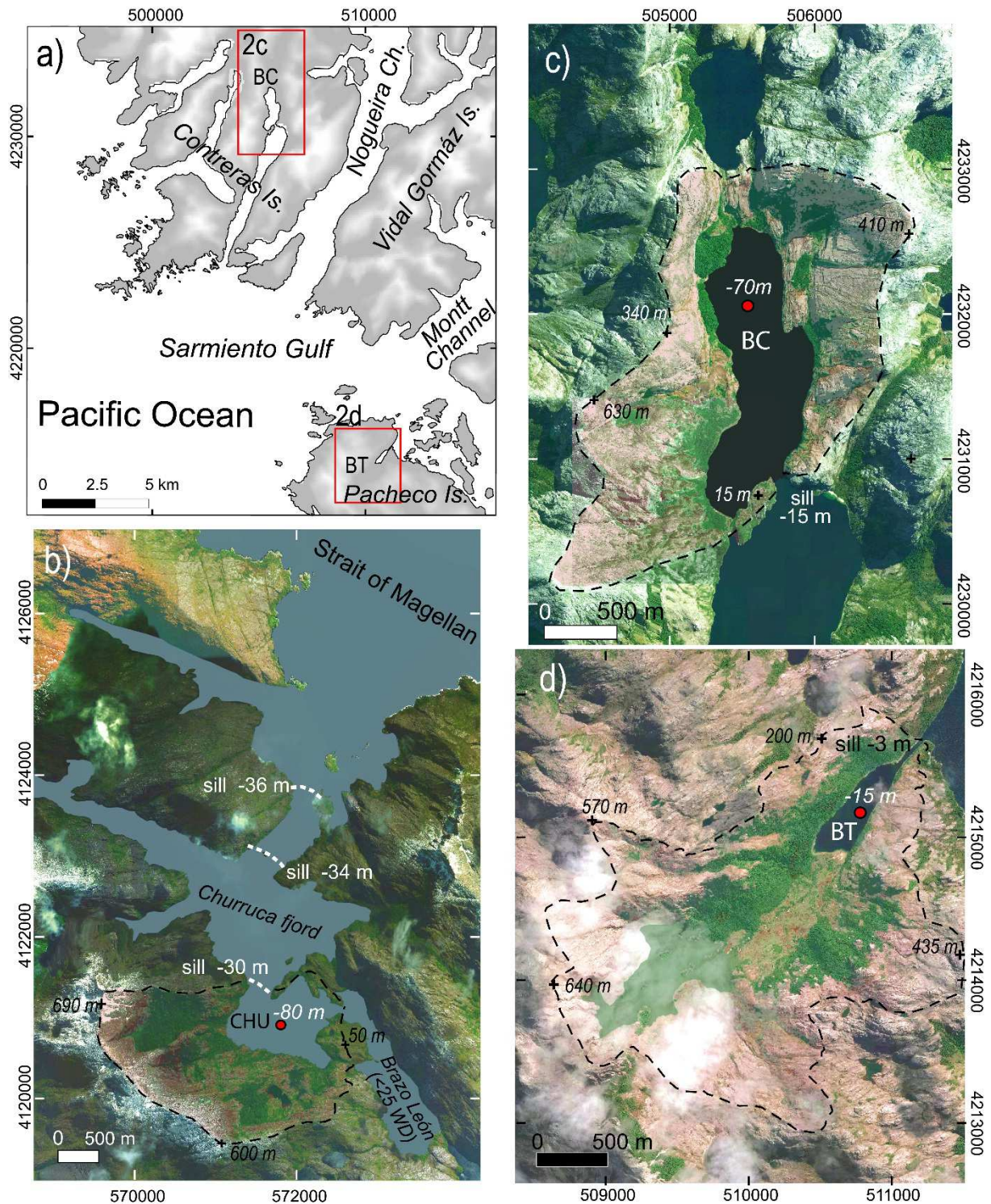
185 The catchment areas of the studied basins are dominated by outcrops of the
186 Southern Patagonian Batholith, including plutonites with a composition from granite to
187 gabbro and mafic dikes (Diaz-Michelena and Kilian, 2015; Hervé et al., 2007). Carbonate
188 rocks are absent in the catchment and in the areas surrounding the studied sites. The closest
189 limestone outcrops are located >70 km northward from the coastal sites BT and BC on Diego
190 de Almagro Island (Fig.1 and Suppl. fig. S1). The vegetation is composed by rain forest
191 patches in favorable sites with adequate drainage and shelter from wind. In sectors with
192 lower slopes, such as in BT and CHU, there is also development of dwarf shrubs, grass and
193 herbs.

194 Figure 2b illustrates the multi-basin estuary of the Churruca fjord where one of the
195 investigated sites is located (CHU). The main basin has a N-S orientation from mouth to
196 head. The three main arms are oriented NW-SE following the structural fabrics of the rocks
197 along the Magellan-Fagnano fault system (Breuer et al., 2013b). The water exchange with
198 the Strait of Magellan is restricted by two sills (<36 m and <34 m water depth, WD)
199 separating the inner and outer fjord. In the inner fjord area, a shallow contraction (<30 m
200 WD) further restricts the water exchange between the fjord's inner and outer sub-basins.

201 Towards the head of the estuary, a narrow constriction separates the shallow Brazo León
202 sub-basin (<25 m WD, Fig. 2b) from the deeper outer basins. The southwestern flanks of the
203 surrounding mountains are up to 650 m high with slope angles of 15° to 25°. Physical
204 characteristics are summarized in Table1.

205 The Bahía Caribe site (BC) is located in a semi-elliptic basin with a N-S orientation
206 located at the head of an elongated fjord in ENE-WSW direction (Figs. 2a and 2c). The water
207 exchange is restricted by a sill of 15 m WD, which connects the basin with a narrow inlet (7
208 km length, 0.5 km width, 200–250 m WD) open to the Pacific Ocean. The freshwater inflow
209 comes from runoff and from a small affluent at the head of the fjord. During the coring
210 operation (austral spring), a very low salinity was measured at the surface (3 psu) increasing
211 strongly with depth to 30 psu at 6 m WD, from where values of 31 psu remained constant
212 until the bottom at 70 m WD. Both east and west flanks of this basin display steep slopes
213 (30° to 50°) with a restricted vegetation cover (Table 1). The lower elevations of the
214 catchment, particularly on the western flank, are characterized by well drained clastic slope
215 deposits and almost totally covered by dense rainforest (Fig. 2c).

216 The Bahia Trampa site (BT) is a small semi-enclosed shallow bay of 15 m WD with
217 estuarine conditions (Fig. 2d). It has an elongated shape in NE-SW direction and covers a
218 comparatively smaller area than the other sites (Table 1). Towards the northeast, a narrow
219 channel (30 m wide and 230 m long) connects BT with the open fjord system next to the
220 Pacific Ocean. The very shallow depth of this channel (1.5 to 3 m) restricts the water
221 exchange with the open fjord depending on the tidal water levels. Measured salinities
222 increase from 5 psu at the surface to 30 psu at the bottom of the bay. The southern flank of
223 the catchment reaches up to 50 m elevation and exhibits inclinations of 15°–25° and is
224 sparsely vegetated, while the northern flank has steeper slope angles of 30°–35° and is
225 covered by a dense rainforest (Table 1). At the SW shore, a small river enters the bay (Fig.
226 2d).



227

228 **Figure 2:** Detailed maps of the study areas. Red dots indicate coring sites CHU, BC and BT.229 Water depths of sills and basins are shown as white/black annotations. Black dashed lines
230 refer to catchment areas, and annotations over the line indicate their maximum elevations. a)

231 SW sector of Reina Adelaida Archipelago. Red rectangles show the locations of BC and BT

232 sites. b) Churruca fjord site (CHU) at the south coast of the Strait of Magellan. c) Bahía

233 Caribe core site (BC, Contreras Island) and d) Bahía Trampa core site (BT, Pacheco Island).

234 Projection UTM18S, datum WGS84. Image source Bing Maps - Digital Globe 2015.

235 The geomorphological features of the CHU and BC sites are very similar with respect
 236 to catchment and basin sizes and ratios. However, the steeper slopes probably restrict the
 237 vegetation cover and soil development in BC compared with CHU (Table 1). CHU is
 238 characterized as an inner fjord environment with a well-developed vegetation catchment
 239 while BC represents a coastal basin with more restricted terrestrial organic sources. The BT
 240 site is also close to the open marine environment, but presents a more extended vegetation
 241 cover with a much larger catchment/basin ratio than that of BC (Table 1).

242 **Table 1:** Summary of physical characteristics of the three study sites.

Site	Catchment area (km ²)	Basin area (km ²)	Vegetation area (km ²)	Veg. cover (%)	Catchment /basin area	Veg./ basin area	Sill depth (m a.s.l.)
Bahía Trampa	4.4	0.16	1.9	44	27.5	11.9	-3
Bahía Caribe	3.2	0.94	0.7	20	3.4	0.7	-15
Churruca fjord	3.8	0.95	2.2	55	4	2.3	-30

243

244 2.2. Oceanography and precipitation regime

245 At the latitude of the study area (53°S), the coastal surface water properties are controlled by
 246 the Cape Horn Current (CHC) flowing along the Southern Chilean continental margin from
 247 around 45°S towards the Drake Passage (Fig. 1a; Strub et al., 2019; Lamy et al., 2015).
 248 Oceanic waters enter the Magellan fjord system as saline bottom waters (salinity >33 psu)
 249 below a fresh/brackish surface water layer (salinity 1–32 psu; Aracena et al., 2015; Kilian et
 250 al., 2013a; Palma et al., 2014; Valdenegro and Silva, 2003). The thermohaline properties of
 251 the brackish layer are mainly controlled by a variable amount of freshwater input and the
 252 mixing degree with Pacific waters (Silva and Vargas, 2014). The intensity of this surface
 253 freshening changes on seasonal and weekly scales, in particular e.g. after extremely high
 254 precipitation events or due to glacier meltwater loaded with glacial clays and snow melting
 255 that accumulated on top of adjacent mountains. Surface salinities are generally higher during
 256 autumn and winter, while runoff from frequent storms and glacier melting can strongly reduce
 257 salinities (<20 psu) during the late spring and summer in the uppermost few meters of the
 258 water column (Kilian et al., 2007a and 2013a).

259 In the study area, precipitation is driven by the SWW (Garreaud, 2009; Garreaud et
 260 al., 2013). The SWW are strongest between 50°–55°S (Lamy et al., 2010; Saunders et al.,
 261 2018). At these latitudes, annual precipitation on the western side of the orographic barrier of
 262 the Andes reaches very high values (3,000–10,000 mm yr⁻¹; Schneider et al., 2003;

263 Weidemann et al., 2018) and decreases strongly towards the east (e.g. 300–400 mm yr⁻¹ in
264 Punta Arenas, Stolpe and Undurraga, 2016).

265 Coastline changes during the Holocene are related to global sea level rise and
266 regional vertical movements of the continental crust. The uplift in the investigated region is
267 mainly associated with subduction-related tectonic deformation (Bentley and McCulloch,
268 2005; Rostami et al., 2000) and isostatic vertical adjustments (McCulloch et al., 2005; Porter
269 et al., 1984). The combination of these factors strongly affected past environmental changes
270 in the Strait of Magellan area, in accordance with the timing and degree of the marine
271 transgressions (Aracena et al., 2015; Kilian et al., 2007a and 2013a).

272 **3. Material and methods**

273 3.1. Sediment coring

274 The sediment cores were retrieved onboard RV *Gran Campo II* during campaigns in 2007
275 (CHU site) and 2011 (BC and BT sites) after systematic sediment echosounding in each
276 basin. An UWITEC piston corer of 5 m length and 63 mm in diameter with internal and
277 removable PVC liners was used for sediment coring. For composite core lengths of more
278 than 5 m, discontinuous drilling was performed. In this case, for the recovery of the deeper
279 core sections, first the sediments were drilled with closed piston corer (piston in place) to a
280 depth determined 1 m above the base of the previously drilled section. The piston corer was
281 then opened (piston released) and 5 additional meters were drilled with sediment recovery.
282 This was done in order to obtain ~1 m overlap of single core sections. Additionally, 0.4 to 1 m
283 long gravity cores were taken to obtain undisturbed records from the uppermost sediment
284 layers. The correlation between single core sections was performed adjusting the sediment
285 depths in agreement with stratigraphic markers observed in the cores and geochemical
286 measurements. The correlation in BT and BC records was controlled by high-resolution X-ray
287 fluorescence scanner data on the split sediment cores (Suppl. figs. S2, S3 and S4).

288 The investigated sediment core from the CHU fjord (53°03.29'S, 73°55.76'W) was
289 retrieved at 80 m WD. Its composite core length is 11.2 m and consists of three piston core
290 sections (30–517 cm, 430–904 cm and 780–1156 cm core depths). No gravity core was
291 taken at this site. Therefore, we assume that 30 cm of the surface sediments were missing
292 during the piston coring operation considering a linear extrapolation of the three uppermost
293 age determinations (see section 3.3) and regional values of sedimentation and accumulation
294 rates during the late Holocene (Kilian and Lamy, 2012). At the BC site (52°04.04'S,
295 74°55.00'W), a total sediment core composite of 9.1 m length was recovered from 70 m WD.
296 The BC record consists of a superficial gravity core (0–25 cm) and two piston core sections
297 (25–420 cm and 420–911 cm core depth). From the deepest sector of the BT (15 m WD,
298 52°12.84'S, 74°50.54'W), a composite sediment core of 9.0 m length was retrieved. The BT

299 record is composed of a superficial gravity core (0–26 cm) and three piston core sections
300 (27–367 cm, 369–509 cm and 521–900 cm core depths).

301 3.2. Age determinations and age-depth models

302 All sediment cores have been inspected for possible tephra layers known to occur in the
303 region. In the CHU record, the 4.15 kyr BP Mt. Burney tephra was identified at 368 cm
304 sediment depth, by means of its chemical composition and SEM-based typical structure of
305 the included pumices (Kilian et al., 2003 and 2013b). The westernmost BT and BC sites
306 seem to be outside of the Holocene tephra distribution areas of the volcanoes Hudson,
307 Aguilera, Reclus and Mt. Burney (Stern, 2008).

308 Accelerator mass spectrometer radiocarbon ages (^{14}C AMS) were determined on
309 plant remains (i.e. wood or leaves) and marine mollusk shells at NOSAMS (Woods Hole
310 Oceanographic Institution, USA), the Department of Earth Systems Sciences of the
311 University of California, Irvine, USA, and MICADAS Laboratory, AWI, Bremerhaven,
312 Germany. Marine shell ages were corrected for a reservoir effect of 500 yr. This reservoir
313 age was estimated by the offset between the well-dated 4.15 kyr BP Mt. Burney tephra and
314 the ^{14}C ages at the CHU core. All radiocarbon ages have been calibrated using SHCal13
315 calibration curve (Table 2; Hogg et al., 2013). Age models and calculations of sedimentation
316 rates (SR in mm yr^{-1}) were performed with CLAM 2.2 software (Blaauw, 2010). All sediment
317 core depths were corrected for virtually instantaneous event layers with >1 cm thickness.
318 Such event layers were not considered in the calculations of sedimentation rates.

319 The age-depth models were based on the composite depths of the cores and the
320 distribution of the calibrated radiocarbon ages (Table 2), using a spline interpolation that
321 considers a smooth factor of 0.3 for BC and BT, and 0.5 for CHU, in order to adjust the SR at
322 the base of the CHU core to values more consistent with regional rates for the early
323 Holocene (Lamy et al., 2010; Kilian and Lamy, 2012; Fig. 3, Table 3). The CHU core depth-
324 age model was based on eleven ^{14}C AMS ages and the 4.15 kyr BP Mt. Burney tephra layer
325 (Kilian et al., 2003, 2013b; Stern, 2008). Beside the tephra, one event layer was identified in
326 CHU core with a total thickness of 12 cm. Three ^{14}C dates (Table 2) allowed to constrain
327 appropriate SR estimations for the BC core. Six event layers were observed in BC core with
328 a total thickness of 48 cm (Fig. 3b). The depth-age model of the BT core was based on six
329 ^{14}C ages (Table 2). In BT were identified 12 event layers with a total thickness of 32 cm
330 (Fig. 3c).

331

332

333 **Table 2:** Radiocarbon ages and calibrated 95% confidence intervals used for the depth-age
 334 models. The SHCal13 curve (Hogg et al., 2013) was used to calibrate the ages. Marine
 335 reservoir age = 500 yrs. UCI = Department of Earth Systems Sciences University of
 336 California, Irvine; OS = National Ocean Sciences Accelerator Mass Spectrometry Facility
 337 (NOSAMS, Woods Hole Oceanographic Institution). AWI = MICADAS Laboratory, Alfred
 338 Wegener Institute.

Core	Core depth (cm)	Laboratory code	¹⁴ C age±error (yr BP)	Material	Cal. 95% confidence intervals (yr BP)
CHU	58	UCIAMS 82045	1325±15	Marine shell	680–770
CHU	78	UCIAMS 82046	1500±20	Marine shell	810–870
CHU	138	UCIAMS 82047	2070±15	Marine shell	1430–1510
CHU	260	UCIAMS 82048	3275±20	Marine shell	2800–3060
CHU	313	UCIAMS 82049	3730±15	Marine shell	3430–3640
CHU	345	UCIAMS 82050	4205±15	Marine shell	4090–4330
CHU	531	UCIAMS 82051	5595±15	Marine shell	5800–5900
CHU	627	UCIAMS 82052	6935±15	Marine shell	7170–7290
CHU	803	OS-74685	8160±35	Wood	8990–9240
CHU	903	OS-74686	8355±20	Wood	9150–9440
CHU	1080	OS-74687	9740±50	Wood	10800–11230
BC	202	UCIAMS 108165	2125±50	Wood	1930–2300
BC	482	AWI 1352.1.1	5417±57	Wood	6000–6280
BC	714	UCIAMS 108166	8260±60	Wood	9020–9400
BT	123.5	UCIAMS 108158	1350±15	<i>Nothofagus</i> sp. leaf	1190–1280
BT	263	UCIAMS 108159	3395±15	Wood	3490–3690
BT	294.5	UCIAMS 108160	3645±20	<i>Nothofagus</i> sp. leaf	3840–3980
BT	534.5	UCIAMS 108161	6470±20	Wood	7290–7420
BT	685.5	UCIAMS 108164	7560±90	Wood	8170–8540
BT	854.5	UCIAMS 108162	10745±45	Wood	12560–12730

339

340 3.3. Geochemical and physical property analyses

341 For geochemical analyses, a volume of ~3 cm³ of sediment was taken every 10 cm core
 342 depth, and additional samples for the event layers. The samples were weighed and dried
 343 overnight at 105 °C. The dry samples were weighed again to calculate dry bulk density
 344 (DBD) using the formula DBD = wt. (dry) g / sample vol. cm³. The elemental concentrations
 345 of total carbon (TC) and total nitrogen (N) were determined with an elemental analyzer
 346 VARIO Element III at the University of Trier, Germany. Previous to the analyses, all samples
 347 were homogenized using an agate mortar and pestle and subsampled into 20–30 mg
 348 portions and placed in tin capsules. The non-carbonate organic carbon (OC) content was

349 determined on a LECO Carbon Sulfur Analyzer (LECO-CS 125) at the Alfred Wegener
350 Institute (AWI), Bremerhaven, Germany. Samples were acidified by direct addition of HCl
351 (1M) and dried at 150°C overnight. Calcium carbonate was calculated according to the
352 formula: $\text{CaCO}_3 = (\text{TC} - \text{OC}) \times 8.333$ with a detection limit of 0.01 wt% of CaCO_3 .

353 Major elements (Si, Al, Ti, Fe, Mn, Mg, Ca, Na and K) were measured by Atomic
354 Absorption Spectrometry (AAS; Varian SpectrAA 220) at the University of Trier. About 100
355 mg of homogenized sediments were dried (105°C) and fused in Platinum skillets with 400 mg
356 of a flux material (mixture of Lithiumtetraborat, Lithiumcarbonate and Lanthanoxide).
357 Produced glass pearls were dissolved in 40 ml HCl (0.5M). Liquids of samples and
358 international standards (MGR-1, SY-2 and JG-2) were measured by AAS. Determined major
359 elements and loss on ignition (1050°C) resulted in sums of 99-101 wt. %.

360 The relative variation in the chemical composition was measured with an ITRAX
361 μXRF scanner (Croudace et al., 2006) at the Leibniz Institute for Baltic Sea Research,
362 Warnemünde (IOW), Germany. This non-destructive measuring technique allows for semi-
363 quantitative geochemical analysis of split sediment cores with a very high spatial resolution.
364 To avoid evaporation, the core halves were covered with an ultrathin plastic foil before being
365 measured. The XRF measurements of the BT and BC cores were carried out every 2 mm
366 and obtained with a molybdenum (Mo) X-ray tube, operated with a voltage of 40 kV, a
367 current of 10 mA, and 15 s exposure time. In addition, the used μXRF core scanner took
368 measurements of the coherent and incoherent scattering that depend on the mineralogical
369 composition, water content, OC content and sediment packing density (Croudace et al.,
370 2006). The ratio of the incoherent-coherent scattering ($\text{MoInc}/\text{MoCoh}$) can be considered as
371 a good approximation for the content of organic matter, but it needs to be validated by
372 absolute OC measurements, in particular for sediment sequences with high OC contents
373 (Chague-Goff et al., 2016; Chawchai et al., 2016). The XRF scanning data for BC and BT
374 were smoothed to 10-cm intervals using a fifty-point running average to compare with the
375 lower resolution OC values.

376 Scanning results of Ti were normalized by dividing the counts by the
377 coherent/incoherent ratio (Compton/Rayleigh scattering) to minimize the effects of organic
378 matter and water content (Davies et al., 2015) and scaled to match the AAS determinations.
379 This element is present in most lithogenic phases and thus is used as a proxy for inorganic
380 siliciclastic terrestrial contents. μXRF coherent/incoherent normalized counts of bromine (Br)
381 were used as tracers for marine derived organic input, since Br has a biophilic behavior and
382 is typically enriched in ocean water with high nutrient contents (Bertrand et al., 2017;
383 Seidenkrantz et al., 2007; Ziegler et al., 2008). Moreover, calibrated values of Ti and Br were
384 used as tracers for terrestrial and aquatic sources, respectively. As the wt% OC and wt% N
385 determinations were carried out in ~10 cm sediment intervals and the scanning data was

386 obtained every 2 mm, the latter dataset was linearly interpolated to the same depth intervals
387 for an appropriate comparison and further calculation of the terrestrial and aquatic fractions.

388 Terrestrial and aquatic-marine OC were calculated from OC contents using a
389 Bayesian mixed model (Smeaton and Austin, 2017) with the FRUIT software (Fernandes et
390 al., 2014). The highest value of calibrated Ti and Br XRF data were used as end-members
391 for the terrestrial and aquatic-marine sources, respectively. Uncertainties were defined as \pm
392 two standard deviation ($\pm 2SD$), assuming a Gaussian distribution. The third tracer was
393 defined by the molar N/C. Terrestrial and aquatic N/C end members followed those given by
394 Lamy et al. (2010): molar N/C = 0.15 ± 0.02 (C/N= 5.9) as the aquatic (micro algal) end-
395 member and N/C = 0.032 ± 0.002 (C/N = 30.3) as the terrestrial (vascular plant) end-
396 member.

397 Accumulation rates (AR in $\text{kg m}^{-2} \text{kyr}^{-1}$) were calculated by multiplying the
398 concentration of each component by the DBD and the SR determined for each sampling
399 interval. In this study, the AR OC_{aq} and AR CaCO_3 are used as proxies of marine
400 paleoproductivity (Aracena et al., 2015; Lamy et al., 2010). Terrestrial OC primarily originates
401 from nearby land sources and its supply into the fjord basins increases with precipitation and
402 runoff. Therefore, we use AR OC_{terr} as a freshwater input proxy (Frank et al., 2015; Lamy et
403 al., 2010) considering the long-term relation of OC_{terr} input with the vegetation colonization
404 and soil development after deglaciation.

405 Additionally, the cores were inspected for remains of macroorganisms (e.g. bivalves,
406 gastropods, plants). Granulometric analysis of bulk sediment samples of the BT core was
407 performed by wet sieving and decantation. Previous to the dissolution with HCl, the sand
408 fraction of selected core intervals was screened under 40X magnification Zeiss stereoscope
409 at University of Trier to characterize biogenic rests and lithogenic phases.

410 **4. Results**

411 **4.1. Sedimentation rates (SR)**

412 The age-depth models of the studied cores give a maximum age of 14.1 kyr BP for the BT
413 core at 9.0 m of sediment with an averaged SR of 0.6 mm yr^{-1} . The BC record has a
414 maximum age of 12.4 kyr BP at 9.1 m sediment depth while CHU record spans over 11.1 kry
415 BP in 11.2 m of sediment with an average SR of 0.7 and 1.0 mm yr^{-1} , respectively.
416 Sedimentation rate estimations are summarized in Table 3. Four event layers, identified in
417 the BT and BC records, show similar ages and might represent the same regional events.
418 Table 4 presents the modeled age for these events with 95% confidence interval.

419

420

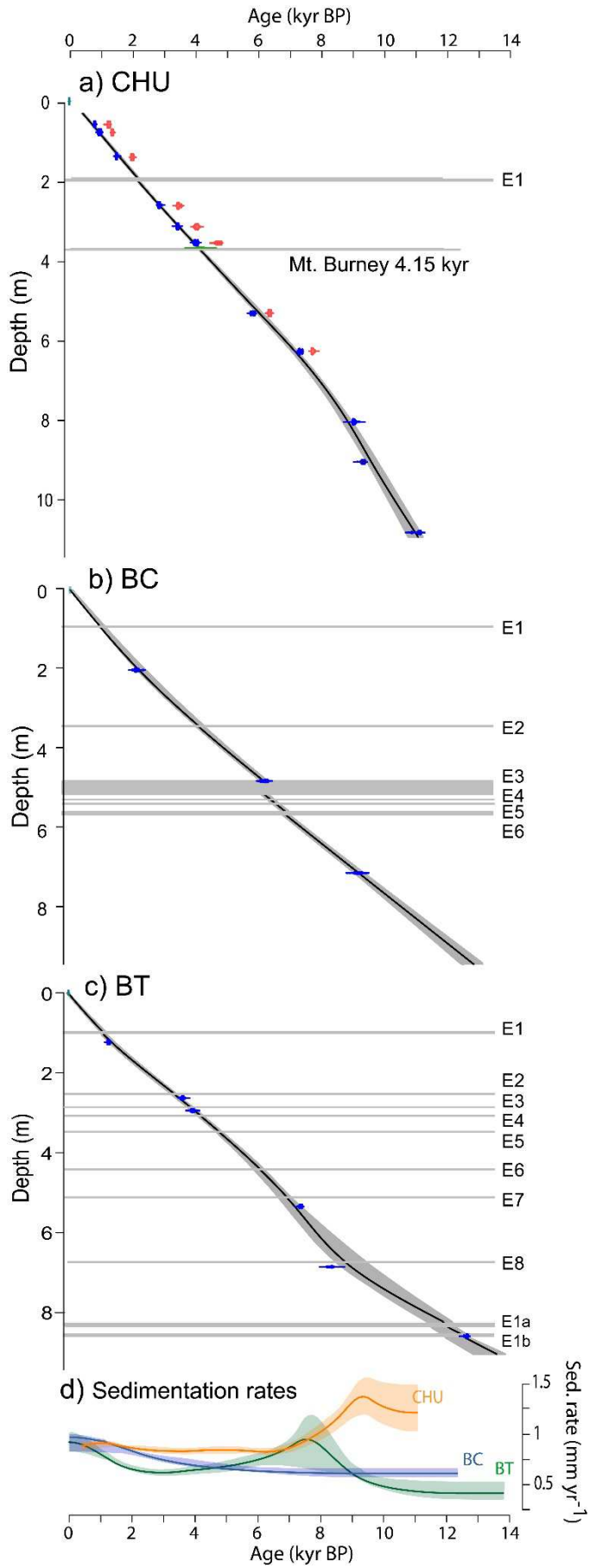
421 **Table 3:** Sedimentation rates (SR) in mm yr^{-1} of the studied cores.

Time interval (kyr BP)	SR 95% confidence intervals (mm yr^{-1})		
	CHU	BC	BT
0 – 5.5	0.8 – 0.9	0.7 – 0.8	0.7 – 0.8
5.5 – 8.5	0.9 – 1.0	0.6 – 0.7	0.7 – 1.0
8.5 – 11.7	1.1 – 1.5	0.6 – 0.7	0.5 – 0.6
> 11.7	-	0.6 – 0.7	0.3 – 0.5

422

423 **Table 4:** Correlation of BC and BT events with 95% confidence interval modeled ages.

BC Core	min. 95%	max. 95%	BT Core	min. 95%	max. 95%
E1	890	1050	E1	970	1150
E2	3970	4230	E3	3850	4020
E3	6040	6260	E6	5850	6170
E6	6660	6880	E7	6630	7050



e-proof

425 **Figure 3:** Age-depth models produced with CLAM 2.2 software. Gray shaded areas indicate
426 95% confidence interval. Horizontal gray lines and annotation indicate single depositional
427 events (Suppl. figs. S2, S3 and S4). Calibrated ^{14}C ages are in blue. a) CHU core with
428 smooth spline factor of 0.5. Red areas indicate the calibrated ages without the reservoir
429 effect correction. For BC and BT cores (b and c) a smooth spline factor of 0.3 was used. d)
430 Sedimentation rates without single depositional events. Colored shaded areas indicate 95%
431 confidence intervals.

432 4.2. Biogenic carbonate concentrations and carbonate fauna

433 The BT core is the only record that includes the Late Glacial since ca. 14 kyr BP and shows
434 laminated inorganic silts with some coarse sand layers until ca. 12.2 kyr BP. The Late Glacial
435 - early Holocene transition is characterized by laminated sediments. After 12.2 kyr BP, a
436 pronounced increase in CaCO_3 is observed (Fig. 4a).

437 Throughout the early Holocene and during the first half of the mid-Holocene, the
438 CaCO_3 content of the three investigated cores steadily increases up to 26 wt%. After the
439 Neoglacial, CHU and BT records exhibit a similar long-term decrease from 25 wt% to 10
440 wt%. In contrast, after ca. 5.5 kyr BP the BC record shows a rapid increase in CaCO_3 content
441 from 14 to 38 wt% and decrease in the last 2 kyr BP (Fig. 4a).

442 Shell fragments of bivalves were identified in the three cores (*Chlamys* sp. and
443 *Desmophyllum* sp.). Identification of benthic foraminifera in the sediments of CHU record
444 showed the presence of *Alveophragmium orbiculatum*, *Bolivina* sp., *Bulimina patagonica*,
445 *Buliminella elegantissima*, *Cibicides dispers*, *Discorbis* sp., *Elphidium* sp., *Stainforthia*
446 *fusiformis*, *Globocassidulina crassa*, *Guttulina communis*, *Lagena caudate*, *Martinotiella*
447 *communis*, *Nonionella auris* and *Spiroloculina tenuis*. BT and BC show less diversity with
448 mainly two taxa, *Buliminella elegantissima* and *Nonionella auris* and more shell fragment of
449 ostracods. Single deposition layers, with coarse sand observed in BT and BC have
450 fragments of echinoderms and a more diverse foraminifer fauna, including, besides
451 *Buliminella* sp. and *Nonionella* sp., *Quinqueloculina seminula*, *Elphidium macellum* and
452 *Cibicides* sp.

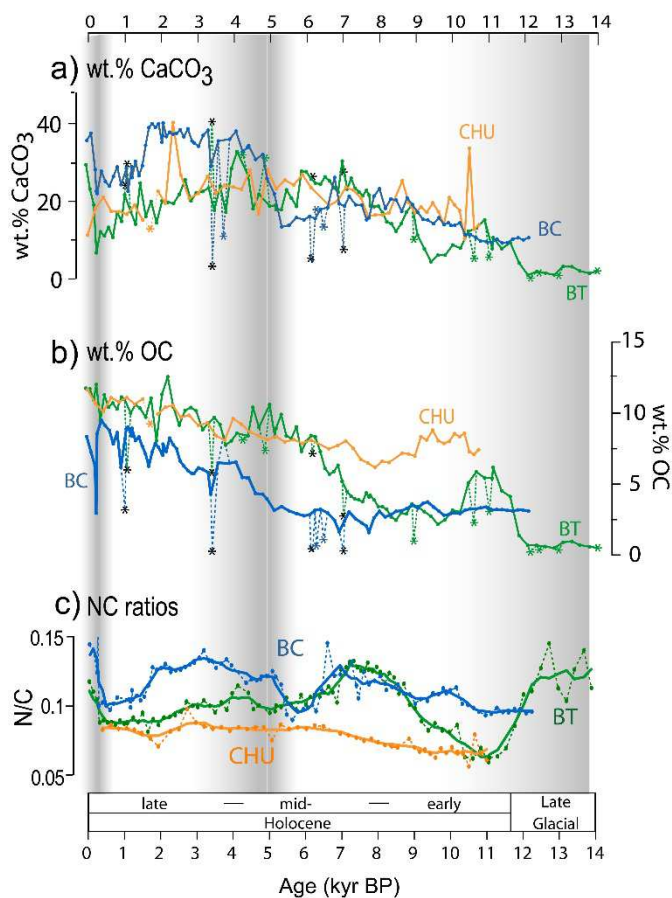
453 4.3. Organic carbon concentration and molar Nitrogen/Carbon

454 Carbon content differs among the studied cores. During the early Holocene, the CHU core
455 shows relatively high OC contents (9 wt%). Wood remains in a debris flow deposit of BT
456 indicate the presence of vegetation within its catchment at least since 12.6 kyr BP; however,
457 the OC content in this record increases after 12.2 kyr BP and reaches similar values as CHU
458 during the mid-Holocene. In contrast, the BC record is characterized by comparatively low
459 contents of OC in the early Holocene, which increases after the Neoglacial (Fig. 4b). In

460 general, all three sites show increasing OC content since the mid-Holocene toward the
461 present.

462 We consider that the incoherent-coherent scattering ratio (MoInc/MoCoh) obtained
463 with the μ XRF core scanner represents a good high resolution proxy for the OC content. The
464 combined datasets from BT and BC cores exhibit very good correlations for the
465 MoInc/MoCoh vs wt% OC ($R^2 = 0.9$, $n = 198$, Suppl. fig. S5).

466 Carbon and nitrogen concentrations are well correlated in the studied cores (Suppl.
467 fig. S6). Molar N/C ratios show different patterns throughout the Holocene. The CHU record
468 displays relatively stable and low N/C ratios, whereas N/C ratios of BC and BT cores are
469 more variable with similar values between ca. 9 and 5.5 kyr BP (Fig. 4c).



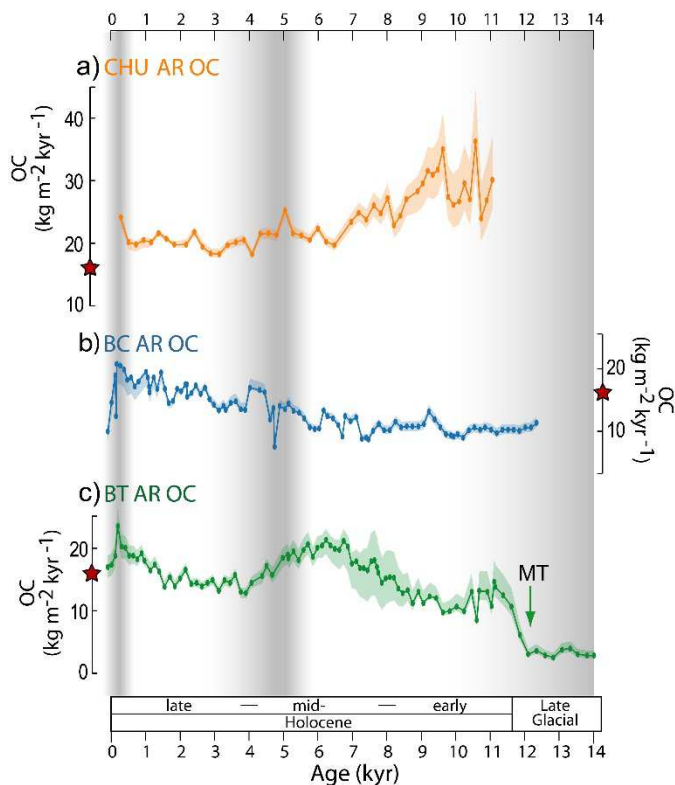
470

471 **Figure 4:** Measured contents of carbon fractions: a) CaCO₃ wt%, b) OC wt% at the studied
472 sites: Churruca fjord (CHU), Bahia Trampa (BT) and Bahia Caribe (BC). Stars indicate layers
473 related to single depositional events. c) N/C molar ratios. Solid line represents a 3 pts.
474 moving average calculated without the values of the single depositional events.

475 4.4. Holocene accumulation rates (AR)

476 4.4.1. Total organic carbon

477 The studied cores show differences in OC accumulation rates. During the early Holocene,
 478 the CHU record is characterized by the highest AR OC ($25\text{--}35 \pm 5 \text{ kg m}^{-2} \text{ kyr}^{-1}$), 2–3 times
 479 higher than the other two cores (Fig. 5a). The BC record shows relatively stable AR OC (Fig.
 480 5b), while the BT record is characterized by the rapid increase in AR OC between ca. 12.0–
 481 11.6 kyr BP from 3 ± 1 to $11 \pm 3 \text{ kg m}^{-2} \text{ kyr}^{-1}$ (Fig. 5c). Towards the mid-Holocene, AR OC in
 482 CHU decreases in $7 \pm 2 \text{ kg m}^{-2} \text{ kyr}^{-1}$ (Fig. 5a), while the BT record shows a net increase in AR
 483 OC of $9 \pm 2 \text{ kg m}^{-2} \text{ kyr}^{-1}$.



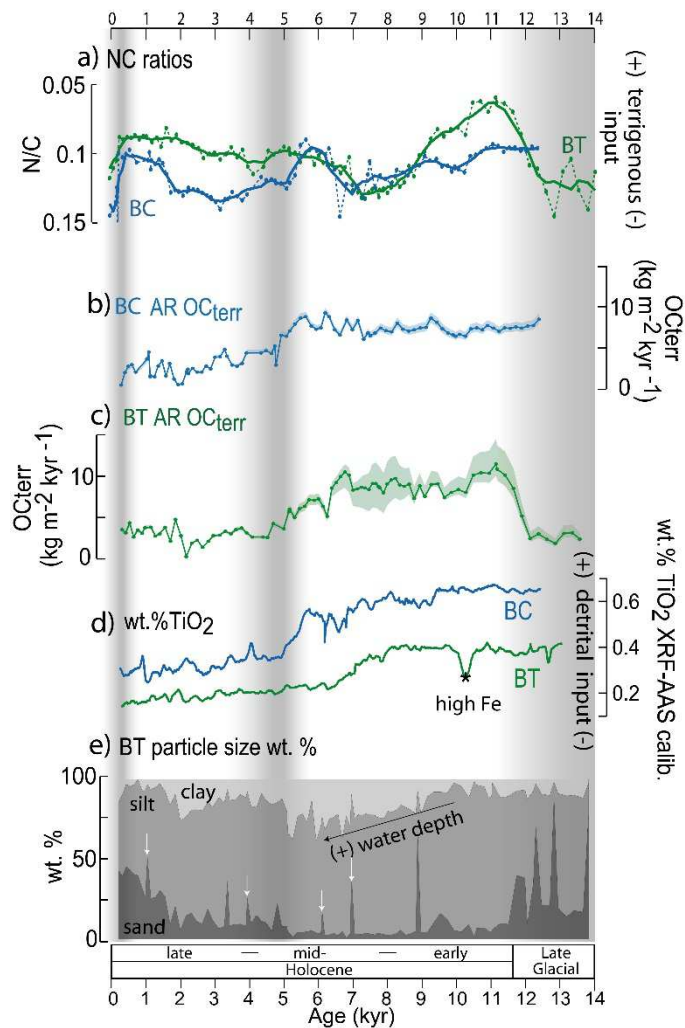
484

485 **Figure 5:** Accumulation rates of organic carbon in the studied cores. Shaded areas indicate
 486 95% confidence interval. Red stars in vertical axes indicate the present-day mean value of
 487 AR OC in Patagonian fjords after Smith et al. (2015). a) CHU, b) BC and c) BT. Green arrow
 488 indicates the marine transgression (MT) in this record. Vertical shaded areas denote cold
 489 periods (Late Glacial, beginning of Neoglacial period and the LIA, Kilian and Lamy, 2012).

490 4.4.2. Terrestrial organic carbon

491 During the early Holocene, BC and BT records indicate predominant accumulation of OC_{terr}
 492 (Fig. 6a and 6b) and relatively high Ti concentrations (Fig. 6c). Throughout the mid-
 493 Holocene, Ti contents and AR OC_{terr} decrease in BT record, while in BC core the decrease in
 494 the Ti contents after 7.5 kyr BP occurred together with relatively stable AR OC_{terr} around
 495 $7.5 \pm 0.5 \text{ kg m}^{-2} \text{ kyr}^{-1}$ (Fig. 6). Coarse bioclastic and siliciclastic depositional events occurred
 496 during the mid-Holocene in the BT and BC cores and they may have had a further influence
 497 on sedimentation dynamics in the records. Particularly in the BT core, the deposition of a
 498 coarse layer at 7.05 kyr BP was followed by an increase in AR OC_{terr} . The onset of the

499 Neoglacial period is characterized by the decrease of AR OC_{terr} and Ti/Al ratios in BC and BT
 500 records (Fig. 6 and Suppl. fig. S8).



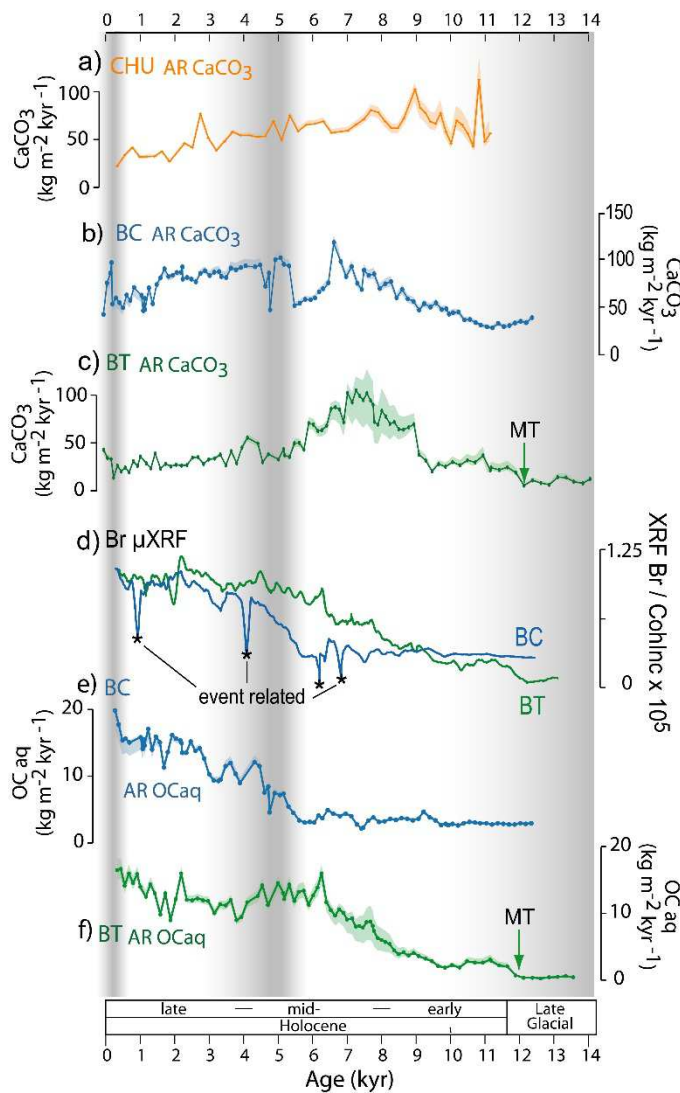
501

502 **Figure 6:** Proxies of terrigenous input to the study sites. a) N/C ratios of BC and BT cores.
 503 Note the inverted scale. b) Accumulation rates of terrestrial carbon in core BC. c)
 504 Accumulation rates of terrestrial carbon in core BT. d) AAS calibrated XRF scanner of the
 505 matrix corrected Ti cps expressed as wt% of TiO_2 in BC and BT cores. The star indicates
 506 high Fe content in BT sediments (Suppl. fig. S7b). e) Particle size distribution in BT core.
 507 White arrows indicate extreme depositional events. Vertical shaded areas denote cold
 508 periods (Late Glacial, beginning of Neoglacial period and LIA, Kilian and Lamy, 2012).

509 4.4.3. Biogenic carbonate and aquatic-marine organic carbon

510 The three sites show an increment in AR $CaCO_3$ during the early Holocene, which continues
 511 throughout the first half of the mid-Holocene in the BC and BT records (Figs. 7a, 7b and 7c).
 512 The rise of AR $CaCO_3$ in the BT core ca. 12.2 kyr BP occurred together with the transition
 513 from inorganic-rich laminated sediments to sediments with laminations of dark-brown/beige
 514 laminae without bioturbation as well as the presence of macroscopic iron sulfide concretions
 515 and high Fe and Mn content. (Suppl. fig. S7b).

516 During the mid-Holocene, AR CaCO_3 of CHU record decreases from 100 ± 9 to 59 ± 2
 517 $\text{kg m}^{-2} \text{kyr}^{-1}$, while BT and BC cores are characterized by a net increase in AR CaCO_3 of 70
 518 $\text{kg m}^{-2} \text{kyr}^{-1}$ between ca. 9.5 and ca. 6.5–7 kyr BP. In the second half of the mid-Holocene,
 519 AR CaCO_3 in BC decreases in similar magnitude as BT, but increases abruptly between 5.5
 520 and 5.3 kyr BP followed by an increment in N/C ratios (Fig. 6a) and Br contents, which are
 521 reflected in the rise of AR OC_{aq} (Figs. 7d and 7e). Thereafter, the three records show an
 522 overall decrease of AR CaCO_3 , which reached a minimum before 0.3 kyr BP. The AR OC_{aq} in
 523 BT record rise gradually until ca. 6.5 kyr BP and decrease slightly after ca. 5.5 kyr BP (Fig.
 524 7f).



525

526 **Figure 7:** Proxies of aquatic productivity at the studied sites. a), b), and c) Accumulation
 527 rates (AR) of CaCO_3 in CHU, BC and BT cores, respectively. d) Matrix-corrected XRF Br cps
 528 of BC and BT cores. Black stars indicate low values related to single depositional events in
 529 BC core. e) Accumulation rates of aquatic organic carbon (OC_{aq}) of BC and f) of BT records.
 530 MT= marine transgression. Vertical shaded areas denote cold periods (Late Glacial,
 531 beginning of Neoglacial period and LIA, Kilian and Lamy, 2012).

532 **5. Discussion**

533 5.1. Holocene sedimentation rates

534 Sedimentation rates (SR) in fjord basins depend on the supply of siliciclastic components,
535 allochthonous OC_{terr} from local catchment areas and local productivity within the water
536 column (Cui et al., 2016; Bertrand et al., 2012 and 2014; Harada et al., 2013; Lamy et al.,
537 2010; Rebolledo et al., 2015 and 2019). Moreover, open fjord systems may also receive a
538 long-distance terrestrial sediment supply (>100 km), often depending on wind-induced
539 surface currents or freshwater runoff within the fjord water surface layer. In particular, glacier
540 sediment discharges can provide extended clay plumes as a major source of allochthonous
541 siliciclastic input (Breuer et al., 2013a; Kilian et al. 2017). Regional and inter-basin variability
542 in Holocene SR at the three sites investigated here suggest that long-distance sediment
543 transport into small enclosed basins either plays no significant role or varies from basin to
544 basin.

545 The relative contribution of terrestrial and aquatic sediment components depends on
546 tidal, climatic and morphological characteristics of the fjords (Hinojosa et al., 2014). In
547 particular, both the relationship of local and/or regional catchments and the areal extent of
548 related basins affect sedimentation and individual accumulation rates of the distinct
549 components (Cui et al., 2017; Smeaton and Austin, 2017; Smeaton et al., 2017). Fjord
550 basins within well definable catchments, as used in this study, have the advantage that past
551 changes in land surface properties (soil and plant development) as well as Holocene
552 coastline evolution can be better constrained.

553 One of the previous studies on Holocene sediments from the Pacific side of the
554 Magellan fjord region comes from a 560 m deep site near Cape Pilar (core PC-03; Harada et
555 al., 2013; Fig. 1b). This core is mainly composed of siliciclastic allochthonous sediments and
556 is characterized by high early Holocene SR, but very low SR during the Neoglacial after 5.5
557 kyr BP. Higher values in the early Holocene have also been reported from shallow bays
558 (<100 m WD; TM1, Palm2 and Par1; Fig. 1b) within the fjord system of the western Strait of
559 Magellan (Kilian et al., 2007b; Lamy et al., 2010).

560 Among the newly investigated sediment cores, only the CHU record shows
561 significantly higher early Holocene SR compared to the late Holocene, whereas the sediment
562 cores BT and BC, located ~100 km north-northwest of CHU and closer to the Pacific coast,
563 show a general subtle increase in SR throughout the Holocene. Relatively higher SR
564 between 8–7 kyr BP in the BT record might be related to the deepening of the basin due to
565 the ongoing marine transgression (MT). The shallower sill at this site probably causes a
566 higher sensitivity of the sedimentation dynamics to sea-level changes compared to the other
567 two sites.

568 Since the glacial retreat in the western Strait of Magellan occurred before ca. 16 kyr
569 (Kilian et al., 2007b), we suggest that the generally higher early Holocene SR observed at
570 many sites (TM1, PAR1, PC-03, Palm2 and CHU; Fig. 1b) may be attributed to a strong input
571 of siliciclastic material and OC_{terr} from the surrounding land areas due to extremely high early
572 Holocene precipitation rates (Lamy et al., 2010; Figs. 5d and 5h) as well as associated
573 outwash of unconsolidated glacial detritus deposited during the Late Glacial (Breuer et al.,
574 2013a). A possible explanation for the comparatively lower early Holocene SR at BC and BT
575 sites is that the coastal area, apart from the ice caps in the inner fjords, may have had less
576 availability of unconsolidated glacial material and less variable precipitation rates between
577 early and late Holocene. Since there is less correlation between wind strength and
578 precipitation in the borders of the SWW and towards the open Pacific (Garreaud et al., 2013),
579 changes in strength, width and position of the SWW zone might have less impact on the
580 precipitation rates in this coastal area, which could have hyper-humid climatic conditions
581 during the whole Holocene.

582 5.2. OC_{terr} supply and vegetation development

583 The N/C-Ti-Br based mass calculation indicate that the contribution of OC_{terr} to the overall
584 OC range is between 20 and 80 wt% at the BC and BT, with higher values during the early
585 and mid-Holocene compared to the late Holocene. The supply of OC_{terr} depends on the
586 relationship between the areas of vegetation-covered catchment and the sediment basin
587 (Smeaton and Austin, 2017). Additionally, changes in precipitation and runoff may also
588 influence the amount of OC_{terr} transported and deposited into fjord and lake basins, partly
589 also during sudden depositional events triggered by earthquakes, volcanic eruptions or
590 extreme precipitation events (Lamy et al., 2010).

591 In the Magellan region, the terrestrial organic matter supply to lakes and fjord basins
592 started after the Late Glacial ice retreat (Kilian and Lamy, 2012). Pollen records from a lake
593 sediment core of Tamar Island (Fig. 1b) indicate a primary plant succession starting after
594 ~15.5 kyr BP, when glaciers retreated towards the Gran Campo Nevado ice cap located 60
595 km further east and the establishment of a dense forest vegetation after ~12 kyr BP (Lamy et
596 al., 2010; Kilian et al., 2007b). The amount of pollen from peat-forming plant communities
597 generally increased throughout the Holocene. Besides climate forcing, this can be partly
598 related to long-term plant succession due to soil development and increasing soil thickness
599 (Biester et al., 2003; Lamy et al., 2010; Yu et al., 2010). Next to Tamar Island, a 3 to 5-fold
600 higher AR OC_{terr} during the early Holocene (compared to the mid- and late Holocene) in fjord
601 cores TM1 and Palm2 has been interpreted as reflecting stronger SWW and higher
602 precipitation that significantly increased the OC transport from terrestrial to aquatic systems
603 (Lamy et al., 2010). This interpretation can be extrapolated to our CHU site, which is
604 characterized by very high AR OC and low N/C ratios during the early Holocene (Fig. 5b).

605 Further evidence for more humid conditions and stronger terrestrial input, and probably a
606 more brackish environment during the early Holocene in Churruca fjord comes from high
607 contributions of freshwater diatoms and the occurrence of chrysophyte cysts (C. Lange,
608 unpublished data). Moreover, the OC input from terrestrial sources could have been
609 enhanced at the CHU site by the transport from the nearby shallow Brazo León, which turned
610 into a fluvial system as an additional catchment area during times of sea level low stand (Fig.
611 2a).

612 5.3. Marine transgression and its effect on water column structure and paleoproductivity

613 The Late Glacial to Holocene eustatic sea level rise (120 m; Lambeck et al., 2014; Fig. 8a)
614 has significantly controlled the coastline evolution globally. In previously glaciated regions
615 eustatic effects are partly superimposed by e.g. isostatic movements. Moreover, in
616 tectonically active region like the Strait of Magellan, vertical movement in the order of several
617 meters, could also have added to the eustatic and isostatic effects (Bentley and McCulloch,
618 2005; Breuer et al., 2013b; De Muro et al., 2018). Although the referenced studies provide
619 some elements of the evolution of the coastline in the western Magellan fjord system and
620 formation of terraces since the LGM, their influence on the aquatic environments in terms of
621 development of e.g. stratified/mixed water columns and local sedimentary systems have not
622 been considered.

623 The investigated bays and fjord have sills at different water depths, which may have
624 controlled the timing of the MT and the influence from open Pacific waters, depending on the
625 isostatic uplift rates. Based on the first occurrence of foraminifera and the increase in AR
626 CaCO_3 in a coastal sediment core next to Tamar Island (TM1, Fig. 1b), Kilian et al. (2007a)
627 suggested a first significant MT in the western Strait of Magellan at 14.3 kyr BP. This was
628 probably related to the rapid sea-level rise during meltwater pulse 1A from -120 to -80 m
629 (Lambeck et al., 2014). The bay of the BC site has at present a deeper sill (15 m WD) and
630 already shows marine conditions at the base of the record at 13 kyr BP, while the shallower-
631 sill site BT documents the MT at ca. 12.2 kyr BP. This suggests that the MT in both BT and
632 BC sites occurred when the global sea level was 60–70 m lower than at present; therefore
633 the Pacific coastline was isostatically depressed by a similar degree at this time (Fig. 8). The
634 preservation of OC-rich laminae in the BT record between ca. 12.2 and 10.4 kyr BP suggests
635 anoxic conditions at the sediment-water interface during this period. The halocline likely
636 established around 12.2 when the marine water started to enter the basin, while the
637 precipitation rates were high (Lamy et al., 2010). The start of brackish conditions in BT is
638 indicated by the increase of AR of CaCO_3 and OC_{aq} and XRF Br content (Fig. 7). After ca.
639 11.7 kyr BP, peaks of Fe and Mn/Ti associated with laminations might be related with
640 alternating sulfidic and oxic water masses since the onset of the MT (Sternbeck and
641 Sohlenius, 1997). The progressive deepening of the BT sill during the early and mid-

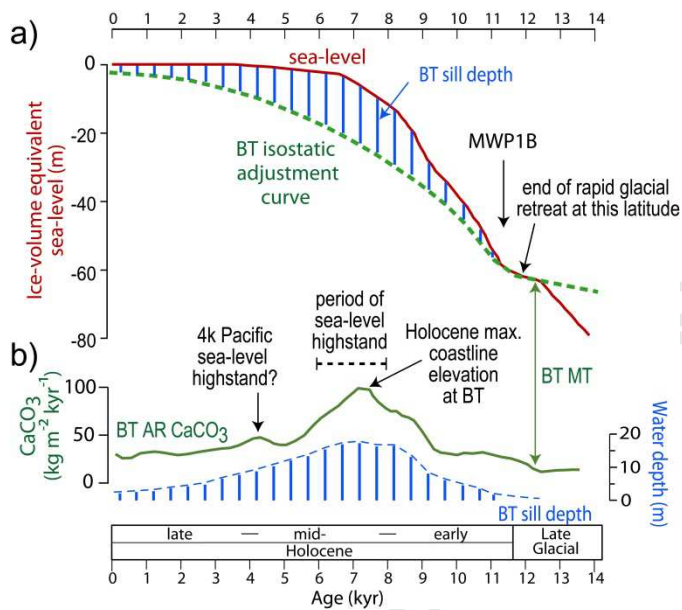
642 Holocene has probably resulted in more mixing in the water column. Further establishment of
643 oxic condition in the sediment-water interface is indicated by remnants of marine organisms
644 (*Chlamys* sp. and *Desmophyllum* sp.; Fig. 9).

645 Records from the central basin of the Strait of Magellan indicate the increment of
646 aquatic productivity after the MT through the Atlantic entrance (cores JPC67, Bertrand et al.,
647 2017, and MD07/3132, Aracena et al., 2015). In both BT and BC cores from the Pacific
648 coast, AR CaCO₃ increased slightly during the early Holocene and reached a maximum
649 between ca. 6.5 and 7 kyr BP (Fig. 7b and 7c). This could be explained by maximum sill
650 depths at this time and a highest coastline elevation. As illustrated in Fig. 8, we suggest that
651 the rates of eustatic rise were higher than the isostatic uplift rates causing a deepening of the
652 sills and increased sea water intrusion into the bays reaching a maximum around 7 kyr BP.
653 Afterwards, the eustatic sea-level stabilized on a global scale, while the local isostatic uplift
654 may have continued slightly. This again could have caused shallower sills at the BT and BC
655 sites reducing the marine influence in the second half of the Holocene. This is e.g., indicated
656 by the decrease in AR CaCO₃ (Fig. 7b and 7c). The long-term decrease of AR CaCO₃ since
657 ca. 7 kyr BP could have been related in general to paleoproductivity changes due to
658 Neoglacial glacier advances and related cold melt water discharge, a reduced degree of MT
659 as discussed above or phases of precipitation-related surface water freshening. The higher
660 sensibility to sea-level changes at BT site might be indicated by the increase in AR CaCO₃
661 around 4 kyr BP, which could be related with the sea-level highstand documented in other
662 areas of the Pacific Ocean (Fig. 8; Chiba et al., 2016; Clement et al., 2016; Miklavič et al.,
663 2018; Yokoyama et al., 2016).

664 Holocene variations in the relative abundance of carbon from different sources in fjord
665 sediments respond to changes in oceanography and sea-level (Knies, 2005; Moossen et al.,
666 2013). At the studied sites, AR CaCO₃ are affected by the enhanced input of marine nutrients
667 by an increasing degree of MT, which is a plausible explanation for the increment in
668 productivity. Cuevas et al. (2019) report that chlorophyll-*a* concentration within the water
669 column is favored by oceanic nutrients in southern Patagonia. Carbonate producer
670 organisms, in particular benthic foraminifera (Pawłowska et al., 2017) have a range of pH
671 tolerance that varies from species to species. Laboratory culture experiments indicate that
672 salinity induced pH changes affect calcification and reproduction in benthic foraminifera. The
673 response to salinity changes is not linear, but with salinities <20 psu the reproduction rate is
674 <3% and salinities <10 psu cause the death of specimens preceded by dissolution of the
675 entire test (Saraswat et al., 2011).

676 Overall accumulation rates of OC in BC and BT are lower than in the CHU record, but
677 still in the same order of magnitude. Our estimates range between 7.5–36.2 g m⁻² y⁻¹, which
678 are comparable with values published from Scotland (3.0–32.1 g m⁻² y⁻¹; Smeaton et al.,

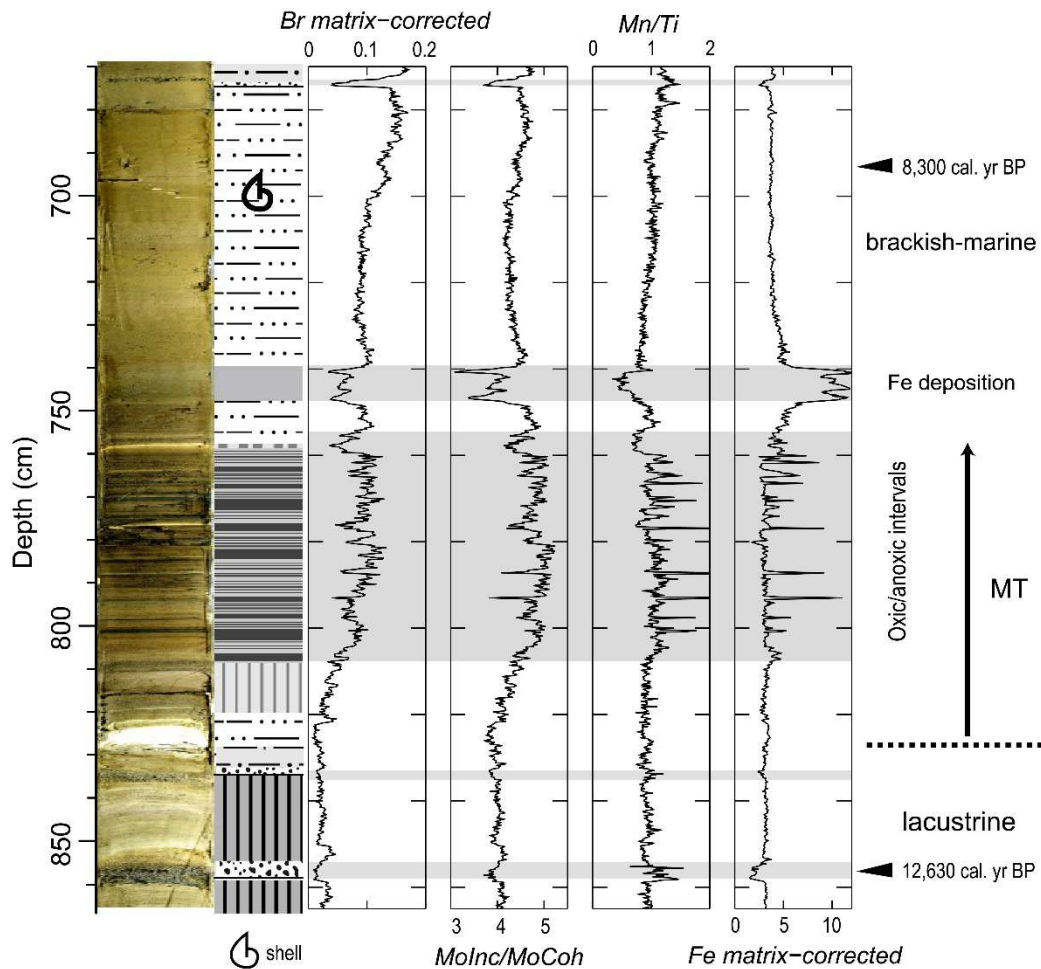
679 2016) and European Arctic Fjords ($20.3\text{--}40.5\text{ g m}^{-2}\text{ yr}^{-1}$; Koziarowska et al., 2018). Other fjord
 680 regions present mean values that are in a similar range, but the upper values are half to one
 681 order of magnitude higher than our estimations, e.g., Northern Patagonia ($1.9\text{--}82.5\text{ g m}^{-2}\text{ yr}^{-1}$;
 682 Sepúlveda et al., 2011), New Zealand ($9.1\text{--}68.0\text{ g m}^{-2}\text{ yr}^{-1}$; Cui et al., 2016; Hinojosa et al.,
 683 2014; Knudson et al., 2011; Smith et al., 2015), Norway ($13\text{--}171\text{ g m}^{-2}\text{ yr}^{-1}$; Duffield et al.,
 684 2017; Faust and Knies, 2018) and Canada ($20\text{--}290\text{ g m}^{-2}\text{ yr}^{-1}$; St-Onge and Hillaire-Marcel,
 685 2001). These values should reflect the spatial heterogeneity of AR OC between fjord
 686 systems, which has been linked with the sediment type and particle size of the seabed
 687 (Smeaton and Austin, 2019).



688

689 **Figure 8:** a) Global sea level rise (red line; Lambeck et al., 2014) and the hypothetical
 690 isostatic adjustment curve at BT site. Depth changes at the basin entrance are indicated with
 691 vertical blue lines. MWP1B: Meltwater pulse 1B. Glacial retreat timing from Kilian and Lamy
 692 (2012). b) CaCO₃ accumulation rates at BT site shown with 4 points moving average
 693 smoothed curve. Length of vertical blue lines refer to changes in water depths at this site sill.
 694 Sea-level highstands of records from the Pacific Ocean (Chiba et al., 2016; Clement et al.,
 695 2016; Miklavič et al., 2018; Yokoyama et al., 2016).

696



697

698 **Figure 9:** Marine transgression in BT record. Photographic mosaic, core description (Suppl.
 699 fig. S4), and XRF proxies (see section 5.3).

700

701 **6. Conclusions**

702 Three new sediment records from shallow coastal bays and fjords from the western sector of
 703 the Strait of Magellan fjord area were used to investigate environmental variability, organic
 704 fluxes and carbon accumulation throughout the Holocene.

705 Despite the relative proximity of the sites, we observe distinct dynamics of terrestrial
 706 carbon accumulation in the three sediment records. These differences are mainly caused by
 707 geomorphological factors. Site CHU can be considered as an inner fjord environment with a
 708 well-developed soil and vegetation catchment. Sites BT and BC represent more open coastal
 709 basins, the first with vegetation and soil cover and the second with very restricted terrestrial
 710 organic sources.

711 The coastal sites present comparatively more constant SR throughout the whole
 712 Holocene, whereas the inner fjord has significantly higher and more variable early Holocene
 713 SR for two possible reasons: 1) coastal sites have less variation in precipitation between

714 early and late Holocene, and 2) the amount of clastic glacial sediments was much higher in
715 the inner fjords proximal to the large glacier systems, while the coastal ice-distal areas
716 provide a reduced stock of glacial sediment supply during the early Holocene. In addition, our
717 results indicate that AR OC_{terr} in coastal areas are particularly sensitive to local parameters,
718 such as catchment/basin area ratio, plant succession and precipitation regime.

719 The results demonstrate that the AR $CaCO_3$ and AR OC_{aq} are indicative of water
720 column structure in particular for the supply of ocean water and the effect of surface water
721 freshening. The timing and magnitude of the marine transition is controlled by the specific sill
722 depths at each site. Between BT and BC records, the sill-depth difference is 12 m. The BC
723 record shows marine conditions at least since *ca.* 13 kyr ago. In BT, major changes in AR
724 $CaCO_3$ and AR OC place the MT at *ca.* 12.2 kyr BP, when the global sea level was 60–70 m
725 lower than today. This implies an isostatic rebound of this magnitude for the area just to the
726 north of the Strait of Magellan entrance. The interaction between sea level and isostatic
727 adjustment during the Holocene plays a major role for the paleoproductivity changes at
728 coastal sites in western Patagonia.

729 **Acknowledgements**

730 We would like to thank three anonymous reviewers for their comments on this paper and
731 helpful suggestions for improvements. This study was funded by project number 111083487
732 (Ki-456/12) and (Ki-456-/9-1) by the German Research Society (Deutsche
733 Forschungsgemeinschaft: DFG). C.B. Lange acknowledges partial support from Chilean
734 grants CONICYT AFB 170006, and CONICYT FONDAF 150100007 and 15150003. We
735 acknowledge logistic and technical support given by Marcelo Arévalo, Carlos Ríos and Erika
736 Mutschke (UMAG, Punta Arenas, Chile).

737 To the memory of Prof. Dr. Rolf Kilian for his indefatigable efforts and huge contribution to
738 the knowledge of the Patagonian fjords system.

739

740

741 **7. References**

- 742 Aracena, C., Lange, C.B., Iriarte, J.L., Rebolledo, L., Pantoja, S., 2011. Latitudinal patterns of
743 export production recorded in surface sediments of the Chilean Patagonian fjords (41°–
744 55°S) as a response to water column productivity. *Continental Shelf Research*, 31 (3–
745 4): 340–355. <https://doi.org/10.1016/j.csr.2010.08.008>
- 746 Aracena, C., Kilian, R., Lange, C.B., Bertrand, S., Lamy, F., Arz, H.W., De Pol-Holz, R.,
747 Baeza, O., Pantoja, S., Kissel, C., 2015. Holocene variations in productivity associated
748 with changes in glacier activity and freshwater flux in the central basin of the Strait of
749 Magellan. *Palaeogeography, Palaeoclimatology, Palaeoecology*, 436: 112–122.
750 <https://doi.org/10.1016/j.palaeo.2015.06.023>
- 751 Bentley, M., McCulloch, R., 2005. Impact of neotectonics on the record of glacier and sea
752 level fluctuations, Strait of Magellan, Southern Chile. *Geografiska Annaler*, 87 (A):
753 393–402. <https://doi.org/10.1111/j.0435-3676.2005.00265.x>
- 754 Bertrand, S., Huguen, K.A., Sepúlveda, J., Pantoja, S., 2012. Geochemistry of surface
755 sediments from the fjords of Northern Chilean Patagonia (44–47°S): Spatial variability
756 and implications for paleoclimate reconstructions. *Geochimica et Cosmochimica Acta*,
757 76: 125–146. <https://doi.org/10.1016/j.gca.2011.10.028>
- 758 Bertrand, S., Huguen, K.A., Sepúlveda, J., Pantoja, S., 2014. Late Holocene covariability of
759 the southern westerlies and sea surface temperature in northern Chilean Patagonia.
760 *Quaternary Science Reviews*, 105: 195–208.
761 <https://doi.org/10.1016/j.quascirev.2014.09.021>
- 762 Bertrand, S., Lange, C.B., Pantoja, S., Huguen, K., van Tornhout, E.V., Wellner, J.S., 2017.
763 Postglacial fluctuations of Cordillera Darwin glaciers (southernmost Patagonia)
764 reconstructed from Almirantazgo fjord sediments. *Quaternary Science Reviews*, 177:
765 265–275. <https://doi.org/10.1016/j.quascirev.2017.10.029>
- 766 Bianchi, T.S., Arndt, S., Austin, W.E.N., Benn, D.I., Bertrand, S., Cui, X., Faust, J.C.,
767 Koziarowska-Makuch, K., Moy, C.M., Savage, C., Smeaton, C., Smith, R., Syvitski, J.,
768 2020. Fjords as Aquatic Critical Zones (ACZs). *Earth-Science Reviews*, In Press.
769 <https://doi.org/10.1016/j.earscirev.2020.103145>.
- 770 Biester, H., Martinez-Cortizas, A., Birkenstock, S., Kilian, R., 2003. The effect of peat
771 decomposition, and mass loss on historic mercury records in peat bogs from
772 Patagonia. *Environmental Science and Technology*, 37: 32–39.
773 <https://doi.org/10.1021/es025657u>
- 774 Blaauw, M., 2010. Methods and code for 'classical' age-modelling of radiocarbon sequences.
775 *Quaternary Geochronology*, 5: 512–518. <https://doi.org/10.1016/j.quageo.2010.01.002>

- 776 Boyer, T.P., Antonov, J.I., Baranova, O.K., Coleman, C., Garcia, H.E., Grodsky, A., Johnson,
777 D.R., Locarnini, R.A., Mishonov, A.V., O'Brien, T.D., Paver, C.R., Reagan, J.R.,
778 Seidov, D., Smolyar, I.V., Zweng, M. M., 2013. World Ocean Database 2013, NOAA
779 Atlas NESDIS 72, S. Levitus, Ed., A. Mishonov, Technical Ed.; Silver Spring, MD, 209
780 pp. <https://doi.org/10.7289/V5NZ85MT>
- 781 Breuer, S., Kilian, R., Baeza, O., Lamy, F., Arz, H., 2013a. Holocene denudation rates from
782 the superhumid southernmost Chilean Patagonian Andes (53°S) deduced from lake
783 sediment budgets. *Geomorphology*, 164 (2): 135–152.
784 <https://doi.org/10.1016/j.geomorph.2013.01.009>
- 785 Breuer, S., Kilian, R., Schörner, D., Weinrebe, W., Behrmann, J., Baeza, O., 2013b. Glacial
786 and tectonic control on fjord morphology and sediment deposition in the Magellan
787 region (53°S), Chile. *Marine Geology*, 346: 31–46.
788 <https://doi.org/10.1016/j.margeo.2013.07.015>
- 789 Chague-Goff, C., Chan, J.C.H., Goff, J., Gadd, P., 2016. Late Holocene record of
790 environmental changes, cyclones and tsunamis in a coastal lake, Mangaia, Cook
791 Islands. *Island Arc*, 25: 333–349. <https://doi.org/10.1111/iar.12153>
- 792 Chawchai, S., Kylander, M. E., Chabangborn, A., Löwemark, L., Wohlfarth, B., 2016. Testing
793 commonly used X-ray fluorescence core scanning based proxies for organic-rich lake
794 sediments and peat. *Boreas*, 45: 180–189. <https://doi.org/10.1111/bor.12145>
- 795 Chiba, T., Sugihara, S., Matsushima, Y., Arai, Y., Endo, K., 2016. Reconstruction of
796 Holocene relative sea-level change and residual uplift in the lake Inba area, Japan.
797 *Palaeogeography, Palaeoclimatology, Palaeoecology*, 441: 982–996.
798 <https://doi.org/10.1016/j.palaeo.2015.10.042>
- 799 Clement, A.J.H., Whitehouse, P.L., Sloss, C.R., 2016. An examination of spatial variability in
800 the timing and magnitude of Holocene relative sea-level changes in the New Zealand
801 archipelago. *Quaternary Science Reviews*, 131: 73–101.
802 <https://doi.org/10.1016/j.quascirev.2015.09.025>
- 803 Croudace, I.W., Rindby, A., Rothwell, R.G., 2006. ITRAX: Description and Evaluation of a
804 New Multi-function X-ray Core Scanner. In: Geological Society, London, Special
805 Publications, 267 (1): 51–63. <https://doi.org/10.1144/GSL.SP.2006.267.01.04>
- 806 Cuevas, L.A., Tapia, F.J., Iriarte, J.L., González, H.E., Silva, N., Vargas, C.A., 2019.
807 Interplay between freshwater discharge and oceanic waters modulates phytoplankton
808 size-structure in fjords and channel systems of the Chilean Patagonia. *Progress in*
809 *Oceanography*, 173: 103–113. <https://doi.org/10.1016/j.pocean.2019.02.012>

- 810 Cui, X.Q., Bianchi, T.S., Savage, C., Smith, R.W., 2016. Organic carbon burial in fjords:
811 terrestrial versus marine inputs. *Earth and Planetary Science Letters*, 451: 41–50.
812 <https://doi.org/10.1016/j.epsl.2016.07.003>
- 813 Cui, X.Q., Bianchi, T.S., Savage, C., 2017. Erosion of modern terrestrial organic matter as a
814 major component of sediments in fjords. *Geophysical Research Letters*, 44: 1457–
815 1465. <https://doi.org/10.1002/2016GL072260>
- 816 Davies, S.J., Lamb, H.F., Roberts, S.J., 2015. Micro-XRF Core Scanning in Palaeolimnology:
817 Recent Developments. In: *Micro-XRF Studies of Sediment Cores: Applications of a*
818 *non-destructive tool for the environmental sciences* (eds. Croudace, I.W. and Rothwell,
819 R.G.). *Developments in Paleoenvironmental Research* (17): 189–226. Springer.
820 <https://doi.org/10.1007/978-94-017-9849-5>
- 821 De Muro, S., Tecchiato, S., Porta, M., Buosi, C., Ibba, A., 2018. Geomorphology of marine
822 and glacio-lacustrine terraces and raised shorelines in the northern sector of Península
823 Brunswick, Patagonia, Straits of Magellan, Chile. *Journal of Maps*, 14(2): 135–143.
824 <https://doi.org/10.1080/17445647.2018.1441759>
- 825 Diaz-Michelena M., Kilian, R., 2015. Magnetic signatures of the orogenic crust of the
826 Patagonian Andes with implication for planetary exploration. *Physics of the Earth and*
827 *Planetary Interiors*, 248: 35–54. <https://doi.org/10.1016/j.pepi.2015.08.005>
- 828 Duffield, C., Alve, E., Andersen, N., Andersen, T., Hess, S., and Strohmeier, T., 2017. Spatial
829 and temporal organic carbon burial along a fjord to coast transect: A case study from
830 Western Norway, Holocene, 27, 1325–1339.
831 <https://doi.org/10.1177/0959683617690588>
- 832 Faust, J.C., Knies, J., 2019. Organic Matter Sources in North Atlantic Fjord Sediments.
833 *Geochemistry, Geophysics, Geosystems*, 20 (6): 2872–2885.
834 <https://doi.org/10.1029/2019GC008382>
- 835 Fernandes, R., Millard, A. R., Brabec, M., Nadeau, M. J., Grootes, P., 2014. Food
836 reconstruction using isotopic transferred signals (FRUITS): A Bayesian model for diet
837 reconstruction. *PLoS One*, 9(2): 1–9. <https://doi.org/10.1371/journal.pone.0087436>
- 838 Fletcher, M.S., Moreno, P.I., 2012. Have the Southern Westerlies changed in a zonally
839 symmetric manner over the last 14,000 years? A hemisphere-wide take on a
840 controversial problem. *Quaternary International* 276: 299–299.
841 <https://doi.org/10.1016/j.quaint.2011.04.042>
- 842 Frank, D., Reichstein, M., Bahn, M., Thonicke, K., Frank, D., Mahecha, M.D., Smith, P., Van
843 Der Velde, M., Vicca, S., Babst, F., Beer, C., Buchmann, N., Canadell, J.G., Ciais, P.,
844 Cramer, W., Ibrom, A., Miglietta, F., Poulter, B., Ramming, A., Seneviratne, S.I., Walz,

- 845 A., Wattenbach, M., Zavala, M.A., Zscheischler, J., 2015. Effects of climate extremes
846 on the terrestrial carbon cycle: concepts, processes and potential future impacts.
847 *Global Change Biology*, 21: 2861–2880. <https://doi.org/10.1111/gcb.12916>
- 848 Garreaud, R., 2009. The Andes climate and weather. *Advances in Geoscience*, 22: 3–11.
849 <https://doi.org/10.5194/adgeo-22-3-2009>
- 850 Garreaud, R., Lopez, P., Minvielle, M., Rojas M., 2013. Large-Scale Control on the
851 Patagonian Climate. *Journal of Climate*, 26 (1): 215–230. [https://doi.org/10.1175/JCLI-](https://doi.org/10.1175/JCLI-D-12-00001.1)
852 [D-12-00001.1](https://doi.org/10.1175/JCLI-D-12-00001.1)
- 853 González, H.E., Castro, L.R., Daneri, G., Iriarte, J.L., Silva, N., Tapia, F., Teca, E., Vargas,
854 C.A., 2013. Land-ocean gradient in haline stratification and its effects on plankton
855 dynamics and trophic carbon fluxes in Chilean Patagonian fjords (47–50°S). *Progress*
856 *in Oceanography*, 119: 32–47. <https://doi.org/10.1016/j.pocean.2013.06.003>
- 857 González, H.E., Nimptsch, J., Giesecke, R., Silva, N., 2019. Organic matter distribution,
858 composition and its possible fate in the Chilean North-Patagonian estuarine system,
859 *Science of The Total Environment*, 657:1419–1431.
860 <https://doi.org/10.1016/j.scitotenv.2018.11.445>.
- 861 Harada, N., Ninnemann, U., Lange, C.B., Marchant, M., Sato, M., Ahagon, N., Pantoja, S.,
862 2013. Deglacial–Holocene environmental changes at the Pacific entrance of the Strait
863 of Magellan. *Palaeogeography, Palaeoclimatology, Palaeoecology*, 375: 125–135.
864 <https://doi.org/10.1016/j.palaeo.2013.02.022>
- 865 Hinojosa, J.L., Moy, C.M., Stirling, C.H., Wilson, G.S. and Eglinton, T.I., 2014. Carbon
866 cycling and burial in New Zealand's fjords. *Geochemistry, Geophysics, Geosystems*,
867 15 (10): 4047–4063.
- 868 Hervé, F., Pankhurst, R.J., Fanning, C.M., Calderón, M., Yaxley, G.M., 2007. The South
869 Patagonian batholith: 150 my of granite magmatism on a plate margin. *Lithos*, 97: 373–
870 394. <https://doi.org/10.1016/j.lithos.2007.01.007>
- 871 Hogg, A.G., Hua, Q., Blackwell, P.G., Niu, M., Buck, C.E., Guilderson, T.P., Heaton, T.J.,
872 Palmer, J.G., Reimer, P.J., Reimer, R.W., Turney, C.S.M., Zimmerman, S.R.H., 2013.
873 SHCal13 Southern Hemisphere Calibration, 0–50,000 years cal BP. *Radiocarbon*, 55:
874 1889–1903. https://doi.org/10.2458/azu_js_rc.55.16783
- 875 Hromic, T., Ishman, S.D., Silva, N., 2006. Benthic foraminiferal distributions in Chilean fjords:
876 47°S to 54°S. *Marine Micropaleontology*, 59: 115–134.
877 <https://doi.org/10.1016/j.marmicro.2006.02.001>

- 878 Iriarte, J.L., van Ardelan, M., Cuevas, L.A., González, H.E., Sánchez, N., Mykkestad, S.M.,
879 2014. Size-spectrum based differential response of phytoplankton to nutrient and iron-
880 organic matter combinations in microcosm experiments in a Chilean Patagonian Fjord.
881 *Phycological Research*, 62: 136–146. <https://doi.org/10.1111/pre.12050>
- 882 Kilian, R., Lamy, F., 2012. A review of Glacial and Holocene paleoclimate records from
883 southernmost Patagonia (49–55°S). *Quaternary Science Reviews*, 53: 1–23.
884 <https://doi.org/10.1016/j.quascirev.2012.07.017>
- 885 Kilian, R., Hohner, H., Biester, H., Wallrabe-Adams, C., Stern, C., 2003. Holocene peat and
886 lake sediment tephra record from the southernmost Andes (53–55°S). *Revista*
887 *Geológica de Chile*, 30: 47–64. <https://doi.org/10.5027/andgeoV30n1-a02>
- 888 Kilian, R., Biester, H., Behrmann, J., Baeza, O., Fesq-Martin, M., Hohner, M., Schimpf, D.,
889 Friedmann, A., Mangini, A., 2006. Millennium-scale volcanic impact on a superhumid
890 and pristine ecosystem. *Geology*, 34: 609–612. <https://doi.org/10.1130/G22605.1>
- 891 Kilian, R., Baeza, O., Steinke, T., Arevalo, M., Rios, C., Schneider, C., 2007a. Late
892 Pleistocene to Holocene marine transgression and thermohaline control on sediment
893 transport in the western Magellanes fjord system of Chile (53°S). *Quaternary*
894 *International*, 161: 90–107. <https://doi.org/10.1016/j.quaint.2006.10.043>
- 895 Kilian, R., Schneider, C., Koch, J., Fesq-Martin, M., Biester, H., Casassa, G., Arévalo, M.,
896 Wendt, G., Baeza, O., Behrmann, J., 2007b. Palaeoecological constraints on late
897 Glacial and Holocene ice retreat in the Southern Andes (53°S). *Global and Planetary*
898 *Change*, 59: 49–66. <https://doi.org/10.1016/j.gloplacha.2006.11.034>
- 899 Kilian, R., Lamy, F., Arz, H., 2013a. Late Quaternary variations of the southern westerly wind
900 belt and its influences on aquatic ecosystems and glacier extent within the
901 southernmost Andes. *Zeitschrift Der Deutschen Gesellschaft Fur Geowissenschaften*,
902 164: 279–294. <https://doi.org/10.1127/1860-1804/2013/0027>
- 903 Kilian, R., Baeza-Urrea, O., Breuer, S., Ríos, F., Arz, H., Lamy, L., Wirtz, J., Baque, D., Korf,
904 P., Kremer, K., Ríos, C., Mutschke, E., Simon, M., De Pol-Holz, R., Arevalo, M.,
905 Wörner, G., Schneider, C., Casassa, G., 2013b. Late Glacial and Holocene
906 Paleogeographical and Paleocological evolution of the Seno Skyring and Otway
907 fjord systems in the Magellanes Region. *Anales Instituto Patagonia (Chile)*, 41 (2): 7–
908 21. <https://doi.org/10.4067/S0718-686X2013000200001>
- 909 Kilian, R., Breuer, S., Behrmann, J. H., Baeza, O., Diaz-Michelena, M., Mutschke, E., Arz,
910 H.W., Lamy, F., 2017. The Seno Otway pockmark field and its relationship to
911 thermogenic gas occurrence at the western margin of the Magallanes Basin (Chile).
912 *Geo-Marine Letters*, 38 (3): 227–240. <https://doi.org/10.1007/s00367-017-0530-6>

- 913 Knies, J., 2005. Climate-induced changes in sedimentary regimes for organic matter supply
914 on the continental shelf off northern Norway. *Geochimica et Cosmochimica Acta*, 69
915 (19): 4631–4647, doi:10.1016/j.gca.2005.05.014.
- 916 Knudson, K.P., Hendy, I.L., Neil, H.L., 2011. Re-examining Southern Hemisphere westerly
917 wind behavior: Insights from a late Holocene precipitation reconstruction using New
918 Zealand fjord sediments, *Quaternary Science Reviews*, 30 (21–22): 3124–3138,
919 <http://doi:10.1016/j.quascirev.2011.07.017>
- 920 Korup, O., Seidemann, J., Mohr C.H., 2019. Increased landslide activity on forested
921 hillslopes following two recent volcanic eruptions in Chile. *Nature Geoscience*, 12:
922 284–289. <https://doi.org/10.1038/s41561-019-0315-9>
- 923 Koziorowska, K., Kuliński, K., Pempkowiak, J., 2018. Comparison of the burial rate
924 estimation methods of organic and inorganic carbon and quantification of carbon burial
925 in two high Arctic fjords. *Oceanologia* 60 (3): 405–418.
926 <https://doi.org/10.1016/j.oceano.2018.02.005>
- 927 Lambeck, K., Rouby, H., Purcell, A., Sun, Y., Sambridge, M. 2014. Sea level and global ice
928 volumes from the Last Glacial Maximum to the Holocene. *Proceedings of the National*
929 *Academy of Sciences*, 111 (43): 15296–15303
- 930 Lafon L., Silva N., Vargas, C.A., 2014. Contribution of allochthonous organic carbon across
931 the Serrano River Basin and the adjacent fjord system in Southern Chilean Patagonia:
932 insights from the combined use of stable isotopes and fatty acid markers. *Progress in*
933 *Oceanography*, 129: 98–113. <https://doi.org/10.1016/j.pocean.2014.03.004>
- 934 Lamy, F., Kilian, R., Arz, H., Francois, J., Kaiser, J., Prange, M., Steinke, T., 2010. Holocene
935 changes in the position and intensity of the southern westerly wind belt. *Nature*
936 *Geoscience*, 3: 695–699. <https://doi.org/10.1038/NGEO959>
- 937 Lamy, F., Arz, H.W., Kilian, R., Lange, C.B., Lembke-Jene, L., Wengler, M., Kaiser, J.,
938 Baeza-Urrea, O., Hall, I.R., Harada, N., Tiedemann, R., 2015. Glacial reduction and
939 millennial-scale variations in Drake Passage throughflow. *Proceedings of the National*
940 *Academy of Sciences*, 112: 13496–13501. <https://doi.org/10.1073/pnas.1509203112>
- 941 McCulloch, R.D., Bentley, M.J., Tipping, R.M., Clapperton, C.M., 2005. Evidence for late-
942 glacial ice-dammed lakes in the central Strait of Magellan and Bahia Inutil,
943 southernmost South America. *Geografiska Annaler*, 87 (A2): 335–362.
944 <https://doi.org/10.1111/j.0435-3676.2005.00262.x>
- 945 Miklavič, B., Yokoyama, Y., Urata, K., Miyairi, Y., Kan, H., 2018. Holocene relative sea level
946 history from phreatic overgrowths on speleothems (POS) on Minami Daito Island,

- 947 Northern Philippine Sea. *Quaternary International*, 417: 359–368.
948 <https://doi.org/10.1016/j.quaint.2017.09.032>
- 949 Milzer, G., Giraudeau, J., Faust, J., Knies, J., Eynau, F., Rühlemann, C., 2013. Spatial
950 distribution of benthic foraminiferal stable isotopes and dinocyst assemblages in
951 surface sediments of the Trondheimsfjord, central Norway, *Biogeosciences*, 10: 1–16.
952 <https://doi.org/10.5194/bg-10-1-2013>
- 953 Mohr, C.H., Korup, O., Ulloa, H., Iroumé, A., 2017. Pyroclastic eruption boosts organic
954 carbon fluxes into Patagonian fjords. *Global Biogeochemical Cycles*, 31 (11): 1626–
955 1638. <https://doi.org/10.1002/2017GB005647>
- 956 Moossen, H., Abell, R., Quillmann, U., Bendle, J., 2013. Holocene changes in marine
957 productivity and terrestrial organic carbon inputs into an Icelandic fjord: Application of
958 molecular and bulk organic proxies. *The Holocene*, 23 (12): 1699–1710.
959 <https://doi.org/10.1177/0959683613505346>
- 960 Moreno, P.I., Francois, J.P., Moy, C.M., Villa-Martínez, R., 2010. Covariability of the
961 Southern Westerlies and atmospheric CO₂ during the Holocene. *Geology*, 38 (8): 727–
962 730. <https://doi.org/10.1130/G30962.1>
- 963 Nanavati, W.P., Whitlock, C., Iglesias, V., de Porras, M.E., 2019. Postglacial vegetation, fire,
964 and climate history along the eastern Andes, Argentina and Chile (lat. 41–55°S).
965 *Quaternary Science Reviews*, 207: 145–160.
966 <https://doi.org/10.1016/j.quascirev.2019.01.014>.
- 967 New, M., Todd, M., Hulme, M., Jones, P., 2001. Precipitation measurements and trends in
968 the twentieth century. *International Journal of Climatology*, 21: 1922–1999.
969 <https://doi.org/10.1002/joc.680>
- 970 Palma, S., Córdova, P., Silva, N., Silva, C., 2014. Biodiversity and spatial distribution of
971 medusae in the Magellan Region (Southern Patagonian Zone). *Latin American Journal*
972 *of Aquatic Research*, 42 (5): 1175–1188.
- 973 Pantoja, S., Iriarte, J.L., Daneri, G., 2011. Oceanography of the Chilean Patagonia.
974 *Continental Shelf Research*, 31: 149–153. <https://doi.org/10.1016/j.csr.2010.10.013>
- 975 Pawłowska, J., Łącka, M., Kucharska, M., Szymańska, N., Kozirowska, K., Kuliński, K.,
976 Zajaczkowski, M., 2017. Benthic foraminifera contribution to fjord modern carbon pools:
977 a seasonal study in Adventfjorden, Spitsbergen. *Geobiology*, 15 (5): 704–714.
978 <https://doi.org/10.1111/qbi.12242>

- 979 Porter S.C., Stuiver M., Heusser C.J., 1984. Holocene sea-level changes along the Strait of
980 Magellan and Beagle Channel, southernmost South America. *Quaternary Research*,
981 22: 59–67. [http://doi.org/10.1016/0033-5894\(84\)90006-1](http://doi.org/10.1016/0033-5894(84)90006-1).
- 982 Rebolledo, L., Lange, C.B., Bertrand, S., Muñoz, P., Salamanca, M., Lazo, P., Iriarte, J.L.,
983 Vargas, G., Pantoja, S., Dezileau, L., 2015. Late Holocene precipitation variability
984 recorded in the sediments of Reloncaví Fjord (41°S, 72°W), Chile. *Quaternary
985 Research*, 84: 21–36. <https://doi.org/10.1016/j.yqres.2015.05.006>
- 986 Rebolledo, L., Bertrand, S., Lange, C.B., Tapia, F.J., Quiroga, E., Troch, M., Silva, N.,
987 Cárdenas, P., Pantoja, S., 2019. Compositional and biogeochemical variations of
988 sediments across the terrestrial-marine continuum of the Baker-Martínez fjord system
989 (Chile, 48°S). *Progress in Oceanography*, 174: 89–104.
990 <https://doi.org/10.1016/j.pcean.2018.12.004>
- 991 Ríos, F., Kilian, R., Mutschke, E., 2016. Chlorophyll- α thin layers in the Magellan fjord
992 system: The role of the water column stratification. *Continental Shelf Research*, 124: 1–
993 12. <https://doi.org/10.1016/j.csr.2016.04.011>
- 994 Rostami, K., Peltier, W.R., Mangini, A., 2000. Quaternary marine terraces, sea-level changes
995 and uplift history of Patagonia, Argentina: comparisons with predictions of the ICE-4G
996 (VM2) model of the global process of glacial isostatic adjustment. *Quaternary Science
997 Reviews*, 19: 1495–525. doi: 10.1016/S0277-3791(00)00075-5.
- 998 Rüggeberg, A., Flögel, S., W. Dullo, J. Raddatz, V. Liebetrau, 2016. Paleoseawater density
999 reconstruction and its implication for cold-water coral carbonate mounds in the
1000 northeast Atlantic through time. *Paleoceanography*, 31: 1–15.
1001 <https://doi.org/10.1002/2015PA002859>
- 1002 Ryan, W.B.F., Carbotte, S.M., Coplan, J., O'Hara, S., Melkonian, A., Arko, R., Weissel, R.A.,
1003 Ferrini, V., Goodwillie, A., Nitsche, F., Bonczkowski, J., Zemsky, R., 2009. Global Multi-
1004 Resolution Topography (GMRT) synthesis data set. *Geochemistry, Geophysics,
1005 Geosystems*, 10 (3): Q03014. <https://doi.org/10.1029/2008GC002332>
- 1006 Saraswat, R., Kouthanker, M., Kurtarkar, S., Nigam, R., Linshy, V. N., 2011. Effect of salinity
1007 induced pH changes on benthic foraminifera: a laboratory culture experiment,
1008 *Biogeosciences Discussions*, 8: 8423–8450. <https://doi.org/10.5194/bgd-8-8423-2011>,
1009 2011.
- 1010 Saunders, K.M., Roberts, S.J., Perren, B., Butz, C., Sime, L., Davies, S., Van Nieuwenhuyze,
1011 W., Grosjean, M., Hodgson, D.A., 2018. Holocene dynamics of the Southern
1012 Hemisphere westerly winds and possible links to CO₂ outgassing, *Nature Geoscience*,
1013 11: 650–655. <https://doi.org/10.1038/s41561-018-0186-5>

- 1014 Schneider, C., Glaser, M., Kilian, R., Santana, A., Butorovic, N., Casassa, G., 2003. Weather
1015 observations across the Southern Andes at 53°S. *Physical Geography*, 24: 97–119.
1016 <https://doi.org/10.2747/0272-3646.24.2.97>
- 1017 Seidenkrantz, M.-S., Aagaard-Sørensen, S., Sulsbruck, H., Kuijpers, A., Jensen, K. G.,
1018 Kunzendorf, H., 2007. Hydrography and climate change during the last 4,400 years in
1019 Ameralik Fjord, SW Greenland - implications for Labrador Sea palaeoceanography.
1020 *The Holocene*, 17: 387–401. <https://doi.org/10.1177/0959683607075840>
- 1021 Sepúlveda, J., Pantoja, S., Hughen, K. A., 2011. Sources and distribution of organic matter in
1022 northern Patagonia fjords, Chile (~44–47°S): a multi-tracer approach for carbon cycling
1023 assessment. *Continental Shelf Research*, 31: 315–329.
1024 <https://doi.org/10.1016/j.csr.2010.05.013>
- 1025 Silva, N., Vargas, C.A., 2014. Hypoxia in Chilean Patagonian Fjords. *Progress in*
1026 *Oceanography*, 29, 62–74. <https://doi.org/10.1016/j.pocean.2014.05.016>
- 1027 Silva, N., Vargas, C.A., Prego R., 2011. Land-ocean distribution of allochthonous organic
1028 matter in the surface sediments of the Chiloé and Aysén interior seas (Chilean
1029 Northern Patagonia). *Continental Shelf Research*, 31 (3-4): 330–339.
1030 <https://doi.org/10.1016/j.csr.2010.09.009>
- 1031 Smeaton, C., Austin, W.E.N., 2017. Sources, sinks, and subsidies: Terrestrial carbon storage
1032 in mid-latitude fjords. *Journal of Geophysical Research: Biogeosciences*, 122: 2754–
1033 2768. <https://doi.org/10.1002/2017jg003952>
- 1034 Smeaton C., Austin, W.E.N., 2019. Where's the Carbon: Exploring the Spatial Heterogeneity
1035 of Sedimentary Carbon in Mid-Latitude Fjords. *Frontiers in Earth Science*, 7: 269.
1036 <https://doi.org/10.3389/feart.2019.00269>
- 1037 Smeaton, C., Austin, W.E.N., Davies, A.L., Baltzer, A., Abell, R.E., Howe, J.A., 2016.
1038 Substantial stores of sedimentary carbon held in mid-latitude fjords. *Biogeosciences*,
1039 13 (20): 5771–5787. <https://doi.org/10.5194/bg-13-5771-2016>
- 1040 Smeaton, C., Austin, W.E.N., Davies, A.L., Baltzer, A., Howe, J.A., Baxter, J.M., 2017:
1041 Scotland's forgotten carbon: a national assessment of mid-latitude fjord sedimentary
1042 carbon stocks. *Biogeosciences*, 14: 5663–5674. [https://doi.org/10.5194/bg-14-5663-](https://doi.org/10.5194/bg-14-5663-2017)
1043 [2017](https://doi.org/10.5194/bg-14-5663-2017)
- 1044 Smith, R.W., Bianchi T.S., Allison, M., Savage, C., Galy, V., 2015. High rates of organic
1045 carbon burial in fjord sediments globally. *Nature Geoscience*, 8: 450–453.
1046 <https://doi.org/10.1038/ngeo2421>

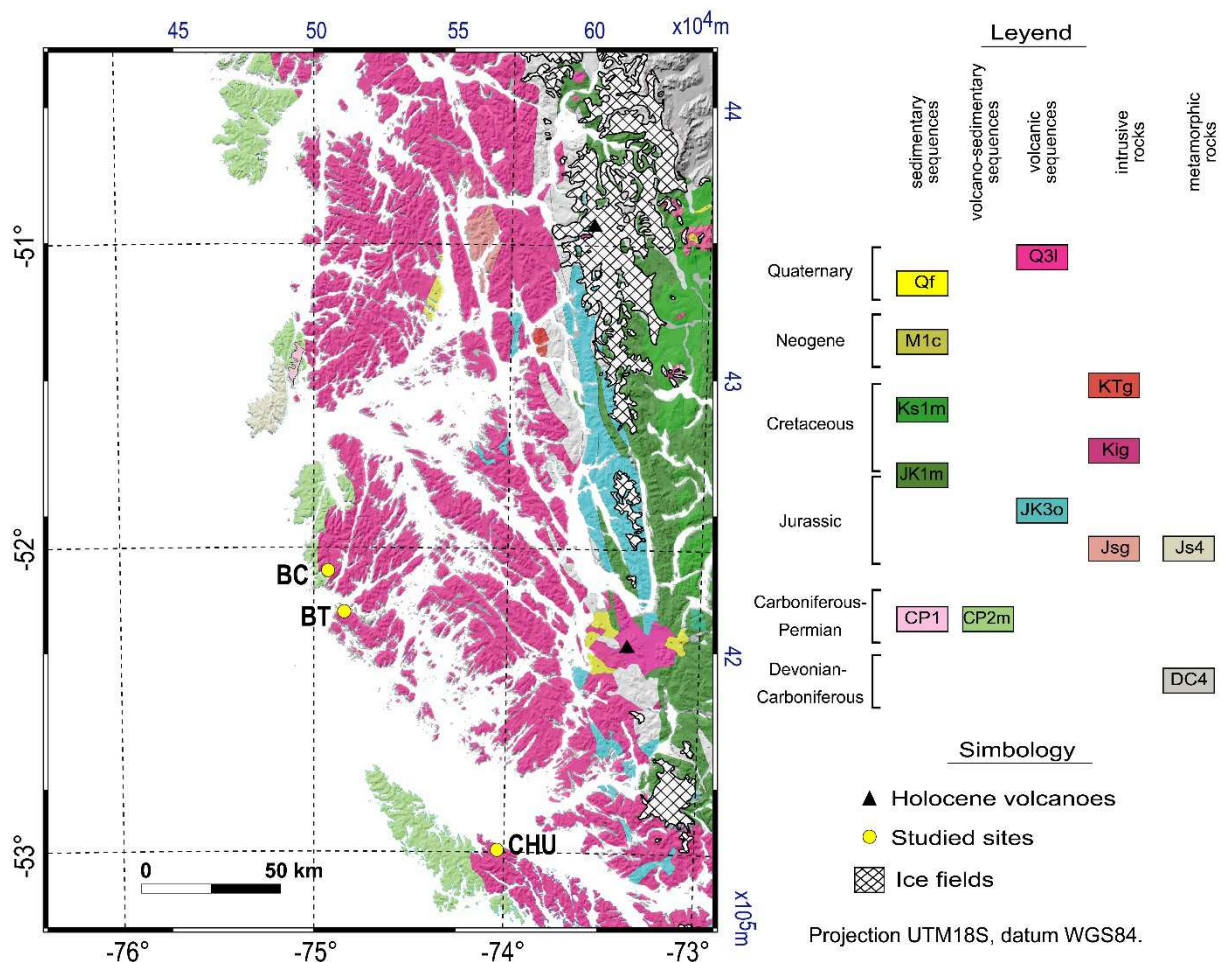
- 1047 Stern, C.R., 2008. Holocene tephrochronology record of large explosive eruptions in the
1048 southernmost Patagonia Andes. *Bulletin of Volcanology*, 70 (4): 435–454.
1049 <https://doi.org/10.1007/s00445-007-0148-z>
- 1050 Sternbeck, J., Sohlenius, G., 1997. Authigenic sulfide and carbonate mineral formation in
1051 Holocene sediments of the Baltic Sea. *Chemical Geology*, 135: 55–73.
- 1052 Stolpe, N., Undurraga, P., 2016. Long term climatic trends in Chile and effects on soil
1053 moisture and temperature regimes. *Chilean Journal of Agricultural Research*, 76 (4):
1054 487–496. <https://doi.org/10.4067/S0718-58392016000400013>
- 1055 St-Onge, G., Hillaire-Marcel, C., 2001. Isotopic constraints of sedimentary inputs and organic
1056 carbon burial rates in the Saguenay Fjord, Quebec. *Marine Geology*, 176: 1–22.
1057 [https://doi.org/10.1016/S0025-3227\(01\)00150-5](https://doi.org/10.1016/S0025-3227(01)00150-5)
- 1058 Strub, P.T., James, C., Montecino, V., Rutllant, J.A., Blanco, J.L., 2019. Ocean circulation
1059 along the southern Chile transition region (38°–46°S): Mean, seasonal and interannual
1060 variability, with a focus on 2014–2016. *Progress in Oceanography*, 172: 159–198.
1061 <https://doi.org/10.1016/j.pocean.2019.01.004>
- 1062 Torres, R., Frangopulos, M., Hamamé, M., Montecino, V., Maureira, C., Pizarro, G., Reid, B.,
1063 Valle-Levinson, A., Blanco, J.L., 2011. Nitrate to silicate ratio variability and the
1064 composition of micro-phytoplankton blooms in the inner-fjord of Seno Ballena (Strait of
1065 Magellan, 54°S). *Continental Shelf Research*, 31 (3–4): 244–253.
1066 <https://doi.org/10.1016/j.csr.2010.07.014>
- 1067 Torres, R., Silva, N., Reid, B., Frangopulos, M., 2014. Silicic acid enrichment of subantarctic
1068 surface water from continental inputs along the Patagonian archipelago interior sea
1069 (41–56°S). *Progress in Oceanography*, 129: 50–61.
1070 <https://doi.org/10.1016/j.pocean.2014.09.008>
- 1071 Valdenegro, A., Silva N., 2003. Caracterización oceanográfica física y química de la zona de
1072 canales y fiordos australes de Chile, entre el estrecho de Magallanes y Cabo de
1073 Hornos (Cimar 3 Fiordos). *Ciencia y Tecnología del Mar*, 26 (2): 19–60.
- 1074 Vargas, C.A., Martinez, R.A., San Martin, V., Aguayo, M., Silva, N., Torres, R., 2011.
1075 Allochthonous subsidies of organic matter across a lake–river–fjord landscape in the
1076 Chilean Patagonia: implications for marine zooplankton in inner fjord areas. *Continental
1077 Shelf Research*, 31: 187–201. <https://doi.org/10.1016/j.csr.2010.06.016>
- 1078 Weidemann, S.S., Sauter, T., Kilian, R., Steger, D., Butorovic, N., Schneider, C., 2018. A 17-
1079 year record of meteorological observations across the Gran Campo Nevado Ice Cap in
1080 Southern Patagonia, Chile, related to synoptic weather types and climate modes.
1081 *Frontiers in Earth Science*, 6: 53. <https://doi.org/10.3389/feart.2018.00053>

- 1082 Yokoyama, Y., Maeda, Y., Okuno, J., Miyairi, Y., Kosuge, T., 2016. Holocene Antarctic
1083 melting and lithospheric uplift history of the southern Okinawa trough inferred from mid
1084 to late-Holocene sea level in Iriomote Island, Ryukyu, Japan. *Quaternary International*,
1085 397: 342–348. <https://doi.org/10.1016/j.quaint.2015.03.030>
- 1086 Yu, Z., Loisel, J., Brosseau, D.P., Beilman, D.W., Hunt, S.J., 2010. Global peatland dynamics
1087 since the Last Glacial Maximum. *Geophysical Research Letters*, 37: L13402.
1088 <https://doi.org/10.1029/2010GL043584>
- 1089 Ziegler, M., Nürnberg, D., Karas, C., Tiedemann, R., Lourens, L.J., 2008. Persistent summer
1090 expansion of the Atlantic Warm Pool during glacial abrupt cold events, *Nature*
1091 *Geoscience*, 1 (9): 601–605. <https://doi.org/10.1038/ngeo277>
- 1092 Zolitschka, B., Fey, M., Janssen, S., Maidana, N.I., Mayr, C., Wulf, S., Haberzettl, T.,
1093 Corbella, H., Lücke, A., Ohlendorf, C., Schäbitz, F., 2019. Southern Hemispheric
1094 westerlies control sedimentary processes of Laguna Azul (south-eastern Patagonia,
1095 Argentina). *The Holocene*, 29: 403–420. <https://doi.org/10.1177/0959683618816446>
- 1096

1097 **Supplementary information to:**1098 “Environmental and coastline changes controlling Holocene carbon accumulation rates in
1099 fjords of the western Strait of Magellan region” by Ríos et al.

1100 Appendix A: Supplementary figures S1 to S8

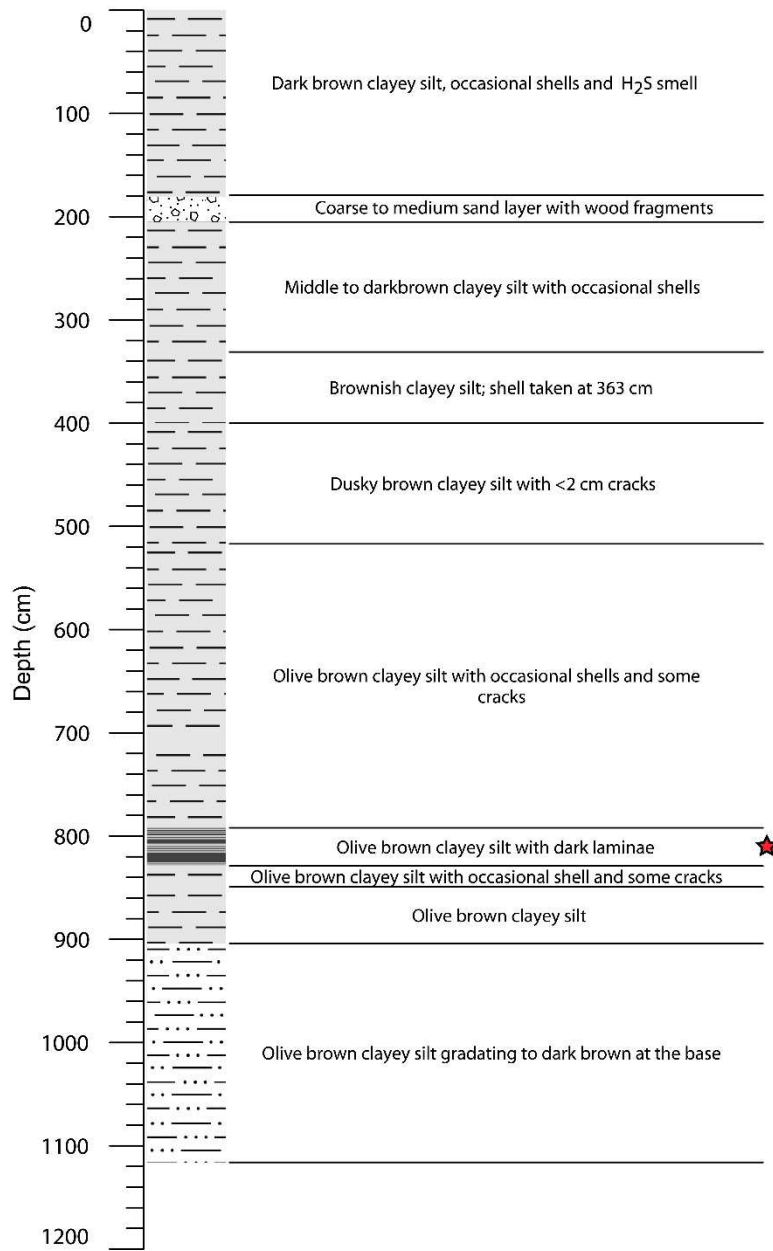
1101 Appendix B: Data repository

1102 **Appendix A. Supplementary figures**

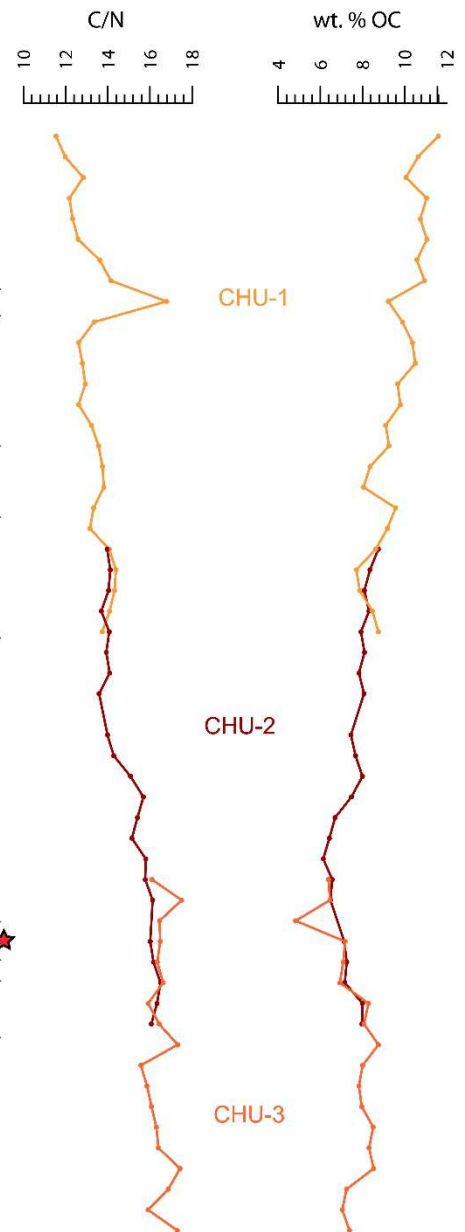
1103

1104 *Figure S1: Geologic map of the study area. Q3l: Monte Burney stratovolcano. Qf: Fluvial*1105 *deposits. M1c: Sedimentary sequences of alluvial or fluvial fans. KTg: Granodiorites,*1106 *diorites and granitic porfids Ks1m: Marine sedimentary sequences. Cerro Toro and Punta*1107 *Barrosa formations. Kig: Granites, granodiorites and tonalites of horblende and biotite.*1108 *JK1m: Marine sedimentary sequences. Zapata formation. JK3o: Sarmiento and Tortuga*1109 *Ophiolite Complexes. Jsg: Quartz-monzodiorites, diorites and granodiorites. Js4: Diego de*1110 *Almagro Metamorphic Complex. Garnet Amphibolites and blueschists, quartz-mica schists*1111 *and orthogneiss. CP1: Tarlton Limestone. Massive limestone and marble. CP2m: Duque*1112 *de York Complex. Sequences of alternating conglomerate, sandstone, and shale beds.*1113 *DC4: Oriental Metamorphic Complex, meta-sandstones. (Hervé et al., 2007; Mpodozis*1114 *and Forsythe, 1983; SERNAGEOMIN, 2003). Blue annotations indicate UTM coordinates.*1115 *Projection UTM18S, datum WGS84.*

a) CHU composite core description



b) CN ratios and wt. % OC correlation between piston core sections

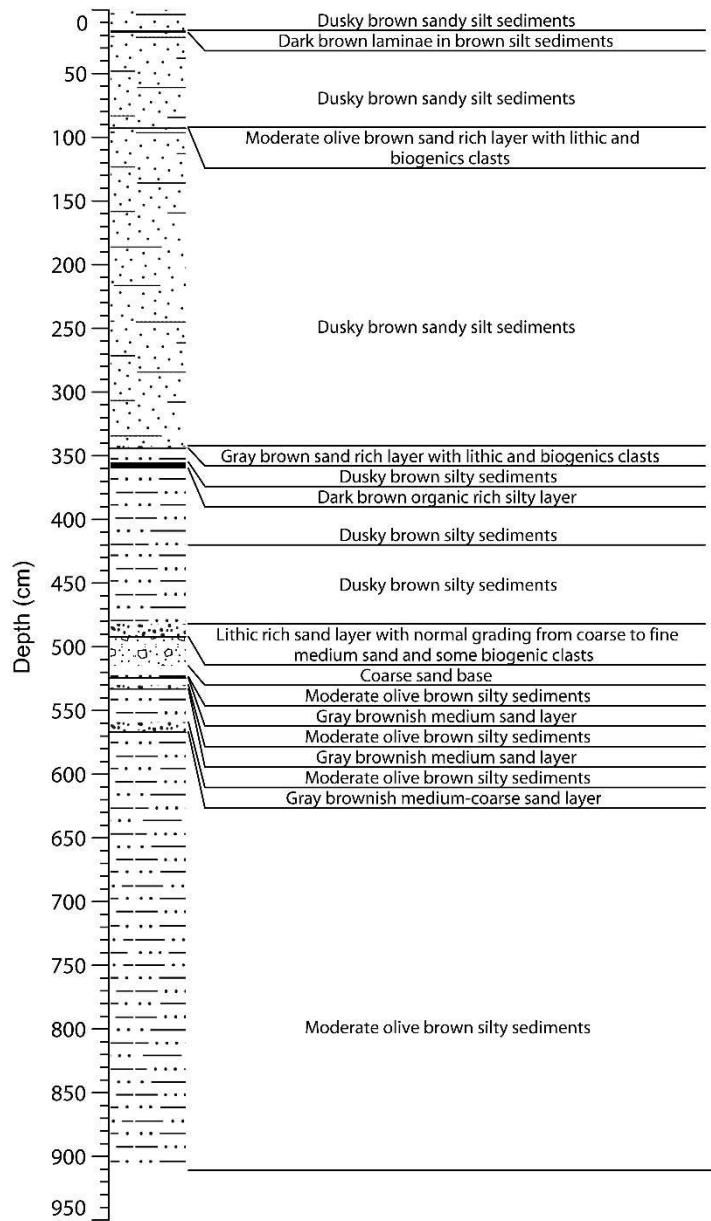


1116

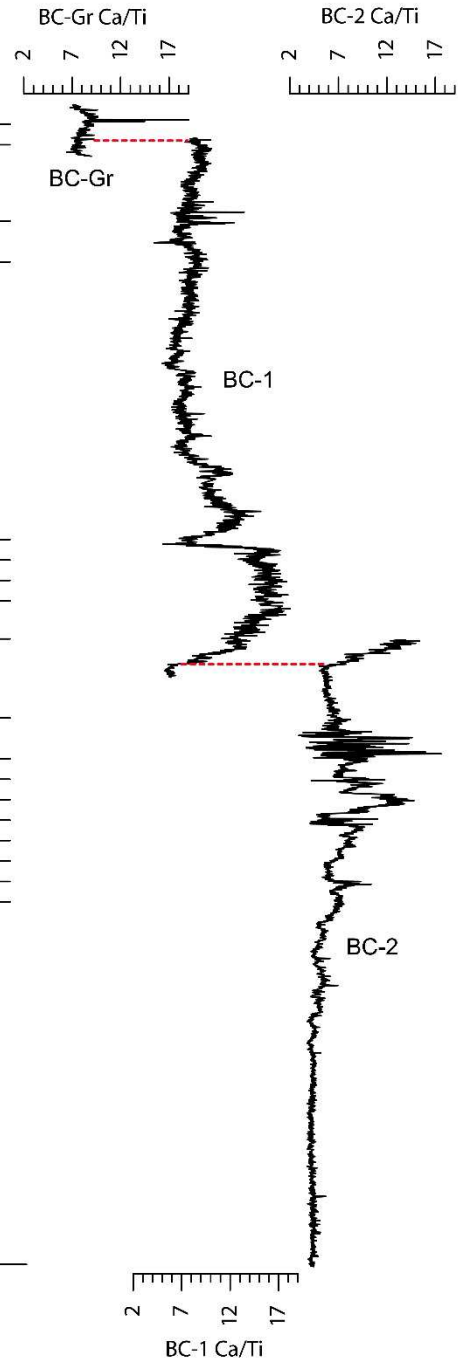
1117 *Figure S2: a) Composite description of core CHU (Churruca fjord). Stratigraphic marker used*
 1118 *for correlation is indicated by a red star. b) Correlation between individual piston sections.*

1119

a) BC composite core description



b) XRF correlation between gravity and piston core sections

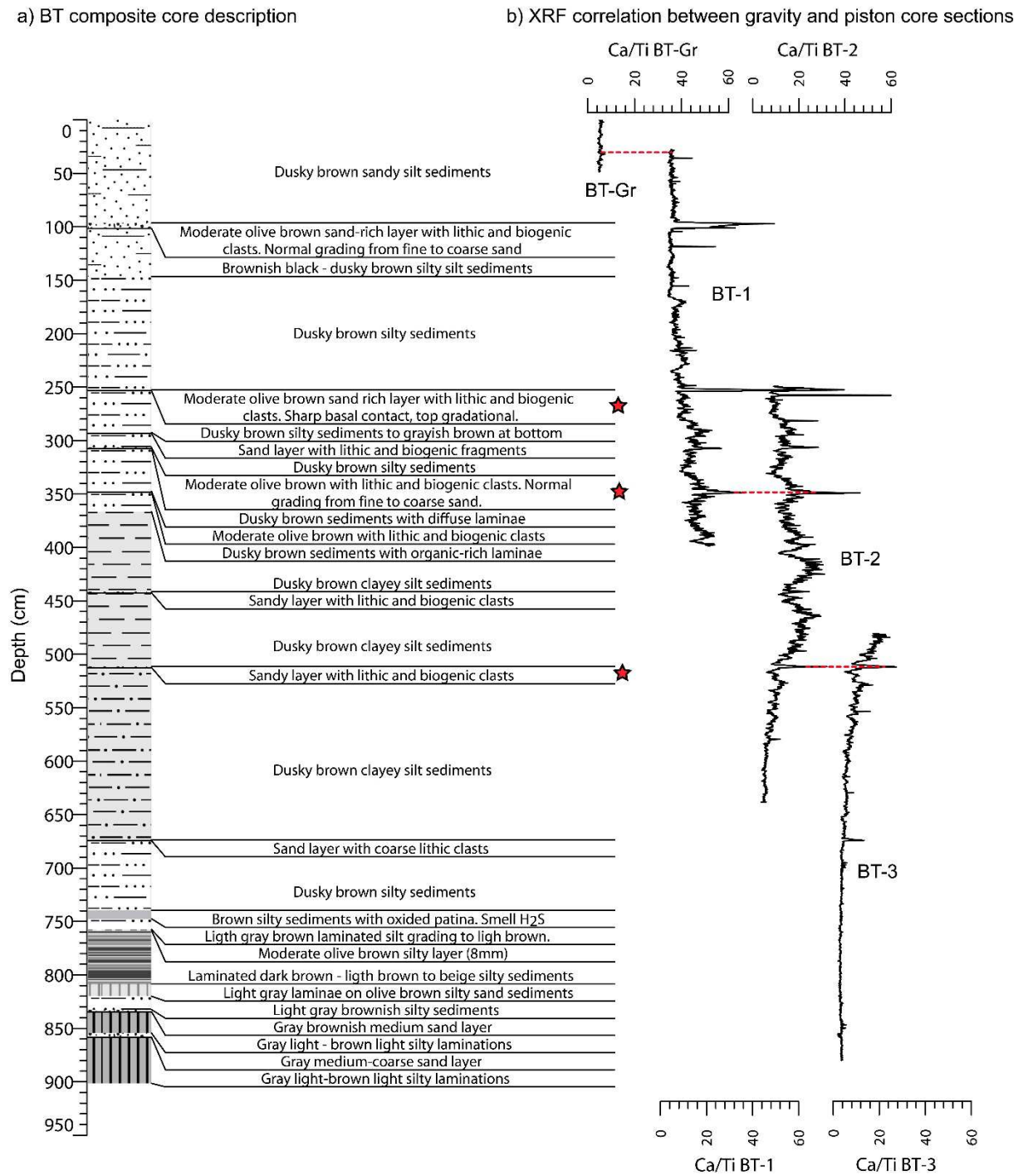


1120

1121 *Figure S3: a) Composite description of core BC (Bahía Caribe). b) Correlation between*1122 *individual piston sections and gravity core.*

1123

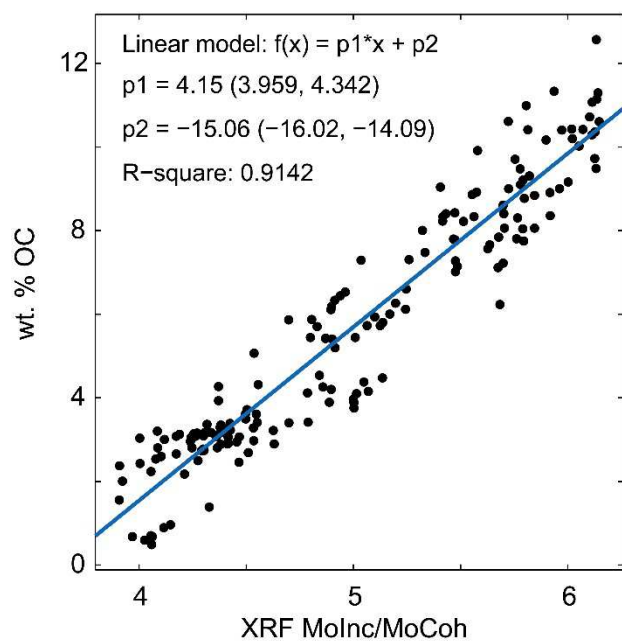
1124



1125

1126 *Figure S4: a) Composite description of core BT (Bahía Trampa). Stratigraphic markers used*
 1127 *for correlation are indicated by red stars. b) Correlation between individual piston sections*
 1128 *and gravity core.*

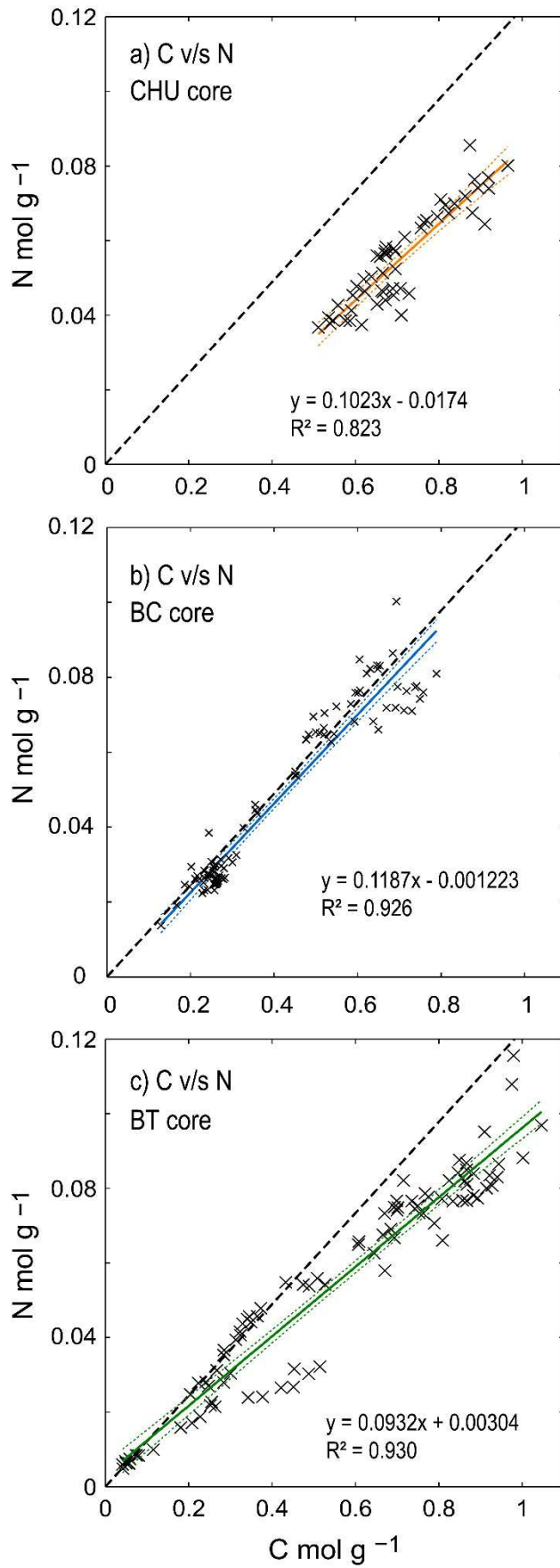
1129



1130

1131 *Figure S5: Correlation diagram between the ratio of the incoherent-coherent scattering*
1132 *(MolInc/MoCoh) vs wt% OC of BT and BC cores. Coefficient values are given with 95%*
1133 *confidence bounds.*

1134

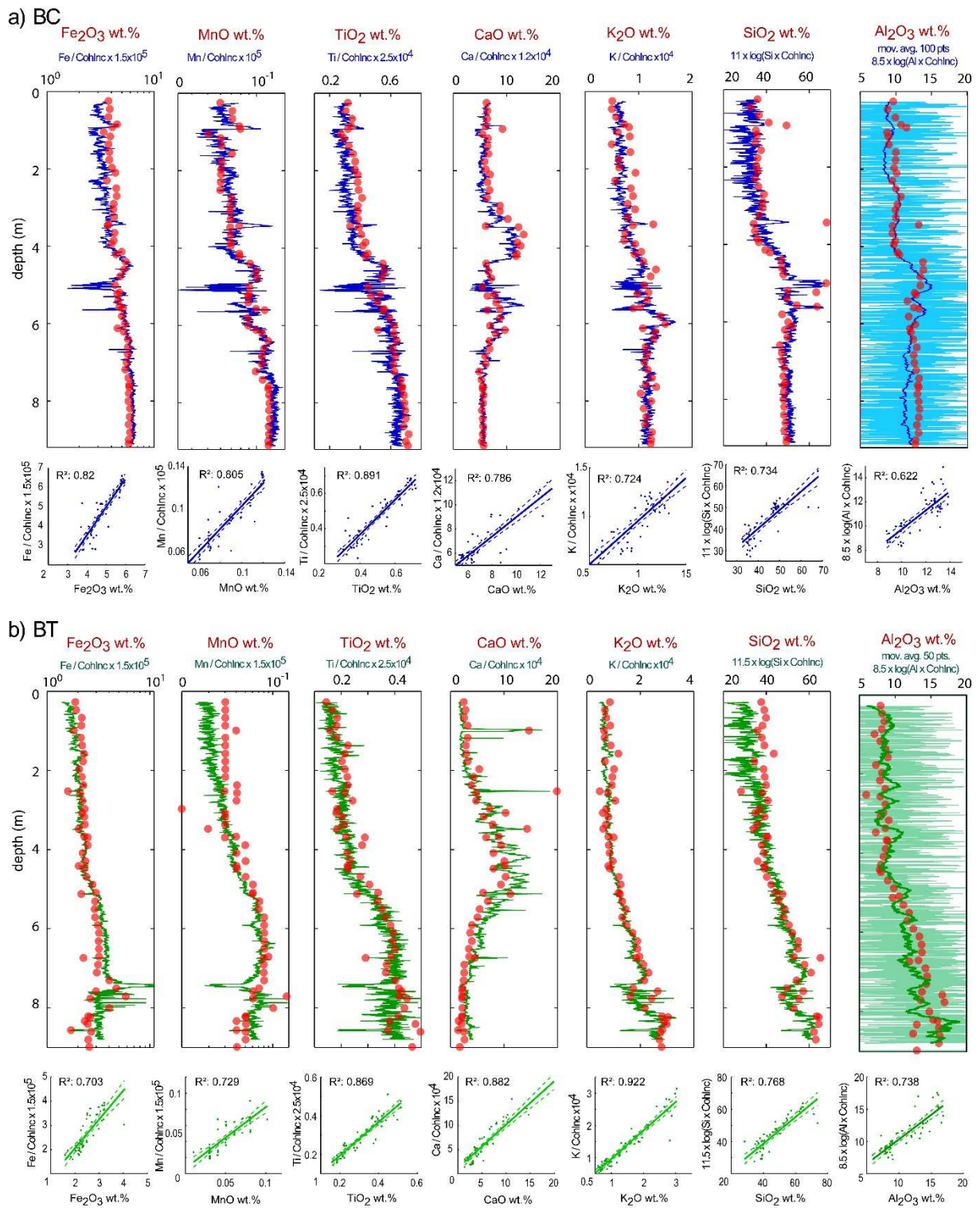


1136 *Figure S6: Linear regression of C and N contents in mol g⁻¹ for a) CHU, b) BC and c) BT*
1137 *records. Black dashed line is the regression line for surface sediment samples from the Strait*
1138 *of Magellan area, after Silva & Ortiz (2002).*

1139

Journal Pre-proof

1140

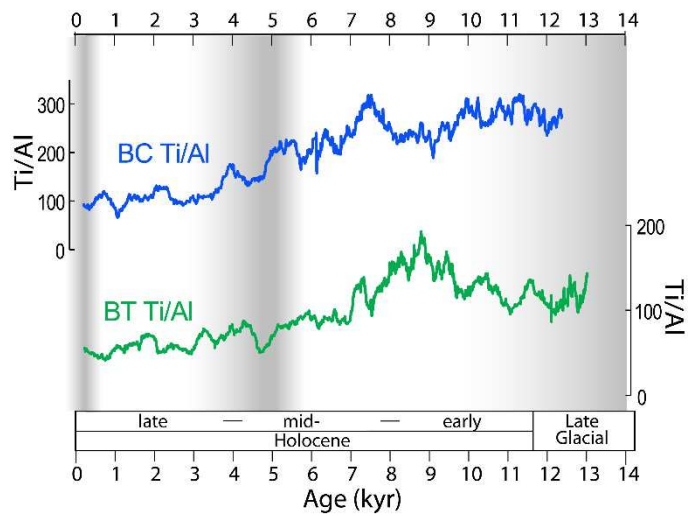


1141

1142 *Figure S7: Geochemical data of BC and BT cores. Blue/green lines show the matrix-*
 1143 *calibrated XRF measurements and red points show the AAS data. Correlation diagrams and*
 1144 *R-square values are shown below each core geochemical measurements.*

1145

1146



1147

1148 *Figure S8: Ti/Al ratios of BC and BT cores*

1149

1150 **References for Appendix A**

1151 Mpodozis, C.; Forsythe, R., 1983. Stratigraphy and geochemistry of accreted fragments of
1152 the ancestral Pacific floor in southern South America. *Palaeogeography, Palaeoclimatology,*
1153 *Palaeoecology*, 41: 103-124.

1154 Silva, N., Ortiz, P., 2002. C y N, su distribución y estequiometría, en sedimentos
1155 superficiales de la región sur de la zona de fiordos y canales australes de Chile, 52° - 56°S
1156 (Crucero CIMAR-fiordo 3). *Ciencia y Tecnología del Mar*, 25 (1): 89-108.

1157

1158

1159 **Appendix B. Supplementary data**

1160 Supplementary data to this article can be found online at

1161 <https://doi.pangaea.de/10.1594/PANGAEA.900790>

Journal Pre-proof

Manuscript “Environmental and coastline changes controlling Holocene carbon accumulation rates in the fjords of the western Strait of Magellan region.”

Highlights

1. Holocene accumulation rates of terrestrial carbon in Patagonian fjords are influenced by local environmental conditions such as precipitation regime, catchment/basin area ratio, and, soil and vegetation development.
2. The accumulation rates of carbonate and aquatic organic carbon in coastal sites with shallow-sills are controlled by the interaction between sea level variations and isostatic adjustments.
3. The marine transgression at Bahia Trampa site indicates a total isostatic rebound of 60–70 m for the north-western Strait of Magellan.